

Article

A Comprehensive Electric Vehicle Model for Vehicle-to-Grid Strategy Development

Fabian Rücker^{1,2,3,*} , Ilka Schoeneberger^{1,2,3}, Till Wilmschen^{1,4}, Ahmed Chahbaz^{1,2,3} , Philipp Dechent^{1,2,3} , Felix Hildenbrand^{1,2,3} , Elias Barbers¹, Matthias Kuipers^{1,2,3}, Jan Figgner^{1,2,3}  and Dirk Uwe Sauer^{1,2,3,5} 

- ¹ Electrochemical Energy Conversion and Storage Systems, Institute for Power Electronics and Electrical Drives (ISEA), RWTH Aachen, Jägerstr. 17-19, 52066 Aachen, Germany; ilka.schoeneberger@isea.rwth-aachen.de (I.S.); till.wilmschen@wallbox.com (T.W.); ahmed.chahbaz@isea.rwth-aachen.de (A.C.); philipp.dechent@isea.rwth-aachen.de (P.D.); felix.hildenbrand@isea.rwth-aachen.de (F.H.); elias.barbers@isea.rwth-aachen.de (E.B.); matthias.kuipers@isea.rwth-aachen.de (M.K.); jan.figgner@isea.rwth-aachen.de (J.F.); dirkuwe.sauer@isea.rwth-aachen.de (D.U.S.)
- ² Juelich Aachen Research Alliance, JARA-Energy, 52056 Aachen, Germany
- ³ Institute for Power Generation and Storage Systems (PGS), E.ON ERC, RWTH Aachen University, Mathieustr. 10, 52074 Aachen, Germany
- ⁴ Wall Box Chargers, S.L., Carrer Josep Ros i Ros, 21, Sant Andreu de la Barca, 08740 Barcelona, Spain
- ⁵ Helmholtz-Institute Münster (HIMS), Ionics in Energy Storage, 52428 Jülich, Germany
- * Correspondence: fabian.ruecker@isea.rwth-aachen.de; Tel.: +49-241-809-6920

Abstract: A comprehensive electric vehicle model is developed to characterize the behavior of the Smart e.d. (2013) while driving, charging and providing vehicle-to-grid services. To facilitate vehicle-to-grid strategy development, the EV model is completed with the measurement of the on-board charger efficiency and the charging control behavior upon external set-point request via IEC 61851-1. The battery model is an electro-thermal model with a dual polarization equivalent circuit electrical model coupled with a lumped thermal model with active liquid cooling. The aging trend of the EV's 50 Ah large format pouch cell with NMC chemistry is evaluated via accelerated aging tests in the laboratory. Performance of the model is validated using laboratory pack tests, charging and driving field data. The RMSE of the cell voltage was between 18.49 mV and 67.17 mV per cell for the validation profiles. Cells stored at 100% SOC and 40 °C reached end-of-life (80% of initial capacity) after 431–589 days. The end-of-life for a cell cycled with 80% DOD around an SOC of 50% is reached after 3634 equivalent full cycles which equates to a driving distance of over 420,000 km. The full parameter set of the model is provided to serve as a resource for vehicle-to-grid strategy development.

Keywords: electric vehicle; battery components; calendar aging; cycle aging; battery model; liquid cooling; charging control; charger efficiency



Citation: Rücker, F.; Schoeneberger, I.; Wilmschen, T.; Chahbaz, A.; Dechent, P.; Hildenbrand, F.; Barbers, E.; Kuipers, M.; Figgner, J.; Sauer, D.U. A Comprehensive Electric Vehicle Model for Vehicle-to-Grid Strategy Development. *Energies* **2022**, *15*, 4186. <https://doi.org/10.3390/en15124186>

Academic Editor: Javier Contreras

Received: 28 April 2022

Accepted: 30 May 2022

Published: 7 June 2022

Publisher's Note: MDPI stays neutral with regard to jurisdictional claims in published maps and institutional affiliations.



Copyright: © 2022 by the authors. Licensee MDPI, Basel, Switzerland. This article is an open access article distributed under the terms and conditions of the Creative Commons Attribution (CC BY) license (<https://creativecommons.org/licenses/by/4.0/>).

1. Introduction

The *Transportation* sector is one of the largest contributors to greenhouse gas (GHG) emissions in the world and is the main cause of air pollution in cities. Therefore, many countries and regions around the world have sketched out pathways and adopted regulations in order to reduce GHG emissions of transportation sector. In the EU, the main elements of the *European Strategy for low-emission mobility* are “Increasing the efficiency of the transport system”, “Speeding up the deployment of low-emission alternative energy for transport” and “Moving towards zero-emission vehicles” [1]. An increased efficiency of the transport system in terms of energy and area use can be achieved with use of railway, public transport systems and the transformation to cyclist and pedestrian friendly urban areas. Examples for low-emission energy alternatives for transport are bio fuels, electricity, renewable synthetic fuels and hydrogen. In the EU, electricity is a low-emission alternative energy as the share of renewable energy in the electricity sector has increased to 34.1% in 2019 [2]. The global

number of electric vehicles (EVs) has increased by 400% from 2016 to 2019 to 4.79 million and is expected to rise in the future [3]. The primary use of EVs is transportation and mobility. However, especially privately owned vehicles but also commercial fleet vehicles are only used for mobility for a small portion of the day. As an example, a privately used vehicle in Germany is parked for 97% of the time [4]. In contrast to privately owned vehicles, commercially used vehicles, such as delivery trucks, tend to have predictable operating and idle times which make them especially interesting for the provision of vehicle-to-grid services. Also, an increasing number of electric delivery vehicles and trucks are registered in the EU [5]. EVs therefore offer the potential for secondary use acting as storage systems connected to an electricity grid or a load. Via an internal or external charger, power can be exchanged with the traction battery of the EV. Several use cases for the secondary use of EVs are being investigated or are already commercially offered. For example, in behind-the-meter use cases an EV can be used as a storage system for on-site energy consumption optimization or an uninterrupted power supply (UPS). For grid services, EVs can also play an important role. They can offer TSO services such as frequency containment reserve and DSO services such as congestion management and power quality improvement. The interplay between EVs and renewable energy sources in grids is extensively studied in order to increase the share of renewable energy and avoid grid congestion. Furthermore, EV chargers can be used to form a microgrid by maintaining its voltage and frequency.

For the simulation of the operation of an EV, an EV model is essential. In the case of the simulation of an EV connected to a grid, the parameterization of the charger and the charging process control is also important. This holds especially true for the development and testing of control algorithms for energy-management systems in order to offer aforementioned services to grid or site operators via vehicle-to-grid (V2G) functionality. In addition, the provision of V2G services adds additional loading to the traction battery of the EV. As the traction battery is an EV's most expensive component, the evaluation of the impact of V2G services on the battery lifetime is important for the economic assessments of such services.

In this paper we parameterize a comprehensive model electric vehicle model for vehicle-to-grid strategy development for the Smart e.d. (2013). The main contributions of this paper are:

- (a) Electro-thermal model of an EV battery pack
- (b) Traction battery break-down (materials, volume and weight distribution)
- (c) Accelerated cycle and calendar aging tests of EV battery cell
- (d) Efficiency measurements of the on-board charger
- (e) Parameterization of the control of the charging process according to IEC 61851-1

Literature Review

Electric vehicles with V2G capability can serve various applications that are being investigated in literature and tested in the field. EVs can participate in existing markets via V2G technology such as energy trading (i.e., spot markets) and frequency control. Furthermore, V2G capability can be utilized to execute behind-the-meter energy flow optimization such as load leveling and peak shaving [6]. Heiltmann and Friedl review factors influencing the economic success of vehicle-to-grid applications in market and behind-the-meter use cases. They find that load leveling and secondary frequency control provide the highest economic benefits for PHEV controlled charging applications [7]. Furthermore, DSO services such as congestion management, power loss minimization, power quality improvement and voltage regulation are topics of investigation for EV participation utilizing V2G technology [8].

The relevant parts of an EV model for V2G applications are the *battery model*, the *charger model* and the *charging control model*.

Battery models in literature have been mainly divided into three categories for the electrical component: Physics-based electrochemical models, equivalent circuit models and data-driven models [9]. In Table 1, we summarize selected literature about li-ion battery and EV modeling with regards to their focus, results and modeled components.

Table 1. Summary of selected literature about li-ion battery and EV modeling.

Source	Date	Focus and Results	Model			Level
			Electrical	Thermal	Aging	
Meshabi et al. [10]	2021	- Electro-thermal model for a LiNiMnCoO ₂ pouch cell with distributed dual polarization (2RC) electrical circuits and distributed thermal (RC) circuits. - Relative error of less than 1.35 °C was achieved in a constant current discharge profile with a 1C rate.	✓	✓	×	Cell
Li et al. [11]	2021	- Modeling of a lithium-ion (LiNiCoAlO ₂) battery pack - 2-D battery pack electro-thermal model with aging, cooling and pack equilibrium management - First order RC electrical model and thermal model considering single cells and cooling system - Genetic algorithm optimization of battery pack charging strategy considering charging time, aging, and energy loss	✓	✓	✓	Pack & Cell
Schmid et al. [12]	2020	- Matrix-vector-based framework for modeling and simulation of EV battery packs with LiNiMnCoO ₂ automotive cells - Dual polarization electrical model (2RC) - Modified Cauer thermal model for each cell in a battery pack and heat transfer between cells, contacts and bus bars of the pack - Holistic aging model for calendar and cycle aging - Model allows for the investigation of three fault cases in the battery pack: Increased contact resistance, external short circuit, internal short circuit	✓	✓	✓	Pack & Cell
Zhu et al. [13]	2019	- Dual polarization electrical model (2RC) of a LiNiMnCoO ₂ cell - Excitation of the battery by inverse binary sequences which eliminates drift of operating conditions and even-order non-linearities - Parameter identification by particle swarm optimization (PSO). The RMSE under the urban dynamometer driving schedule (UDSS) of the terminal voltage was 8.61 mV.	✓	×	×	Cell
Wen et al. [14]	2019	- Dual polarization electrical model (2RC) of a LiNiMnCoO ₂ cell - Parameter identification via recursive least square method with data from pseudo random binary sequence tests - Improved precision for parameters via stochastic theory response reconstruction in contrast to the use of a butterworth filter.	✓	×	×	Cell
Irima et al. [15]	2019	- EV model of a Renault Zoe consisting of the following parts: Vehicle, Driver, Vehicle Control Unit, Electric Motor and Battery. - Two electrical equivalent models: RC model and 3RC Thevenin model. - Simulation of a speed profile with the Simcenter Amesim platform.	✓	×	×	Pack & Cell
Hosseinzadeh et al. [16]	2018	- 1D electrochemical-thermal model of a LiNiMnCoO ₂ pouch cell for an EV. - 3D lumped thermal model of cell. - Decrease of ambient temperature from 45 °C to 5 °C leads to a capacity drop by 17.1% for a 0.5C discharge and a power loss of 7.57% under WLTP drive cycle.	✓	✓	×	Cell
Jafari et al. [17]	2018	- EV battery cycle aging evaluation for driving and vehicle-to-grid services - Cycle aging model for LiFePO ₄ cells with dependency on C-rate, total Ah throughput and temperature	×	×	✓	Cell
Gao et al. [18]	2017	- Measurement of capacity degradation and resistance increase for LiCoO ₂ 18,650 cells - Aging mechanisms are identified via incremental capacity analysis: Loss of active material and loss of lithium inventory. - Overall aging accelerates dramatically for rates over 1C and when the cut-off voltage exceeds 4.2 V. - Establishment of a capacity degradation model.	×	×	✓	Cell
Schmalstieg et al. [19]	2014	- Holistic aging model for LiNiMnCoO ₂ based 18,650 lithium-ion cells - Calendar aging tests for different storage SOCs and temperatures and cycle aging tests for different DODs and average SOCs. - Capacity and inner resistance trend measured with a 1C discharge and pulse power characterization profile respectively. - Electric model consists of series resistance, two ZARC elements and an OCV source parameterized by EIS measurements.	✓	✓	✓	Cell

Physics-based electrochemical models trace back to the work of Newman and Tiedermann [20] and were extended by Fuller [21] for lithium-ion batteries with intercalation. An extensive review of the electrochemical processes in a battery can be found in [22]. In a single-particle model, a radial diffusion equation describes the lithium-ion diffusion in the solid phase of one representative particle for each electrode [23]. In pseudo-two-dimensional (P2D) models each electrode is composed of several spherical particles and the impact of the electrolyte is taken into account. Numerous partial differential equations describe the reactions inside the cell which leads to a large number of unknown variables that need to be identified using global optimization methods.

In electrical equivalent circuit models an electrical circuit is proposed and its components are parameterized through measurements such as impedance spectroscopy, pulse tests and open-circuit voltage (OCV) measurements. Equivalent circuits can vary in their number and type of components which has an impact on the accuracy and computational complexity of the model. The simplest model is the Rint model that consists of an ideal voltage source in series with a resistor [24]. In order to account for transient processes with different time constants such as the charge-transfer and diffusion phenomena, RC networks can be utilized. In [11,25] the Rint model is extended with one RC element.

Other studies use data-driven methods, i.e., machine learning, to parameterize battery models [26–28]. Further studies also model the hysteresis behavior of the OCV of lithium-ion batteries as was done in [29] for LiCoO₂ cells and in [30] for LiFePO₄ cells. In the study conducted by Tran et al. the hysteresis effect was stronger in lithium-ion batteries with LFP and NCA chemistry compared to NMC and LMO chemistry [31]. In addition to integer-order models also fractional-order models are used for equivalent circuit models, which can offer 15–30% higher accuracy than their integer-order analogues but add complexity [32]. Electrical battery models are coupled with thermal models as the electrical parameters, such as the inner resistance, are temperature dependent. An example for the coupling of a thermal 3D model with a P2D model can be found in [33]. Yang et al. employ machine based learning to the thermal parameterization of EV Li-Ion batteries from external short circuit experiments [34]. In this study we choose to parameterize a electrical dual polarization electrical model (2RC) in order to achieve a good trade-off between computational complexity and accuracy for charging processes and dynamic vehicle-to-grid profiles.

In addition to an electro-thermal battery model, an aging model of the traction battery is relevant for EV simulation models. We conduct accelerated cycle and calendar aging tests and evaluate the aging trend with periodic check ups which include a capacity test (full discharge), impedance spectroscopy and pulse tests. This approach was also carried out by Ecker et al [35,36]. In [37] the authors used differential voltage analysis in order to evaluate calendar and cycle aging of a LiFePO₄ cell. Further extensions of a battery model treat mechanical stress during charging and discharging [38,39] or lithium-plating [40].

Within the AVTE project, conducted in the US, numerous EVs were operated and extensively tested. Among others, also the Smart e.d. was tested. The researchers conducted battery tests, such as static capacity tests and pulse power characterization tests along the lifetime of the EV. After two years of operation and 19,000 km the traction battery of the Smart e.d. lost 6.6 % of its capacity and 15.9 % of its 30 s discharge power capability at 80 % depth-of-discharge (DOD) [41]. For an EV model for V2G applications a *charger model* and a *charging control model* are essential components.

In [42], the authors developed an on-board charger prototype that achieves a peak efficiency value of 97.3 % in boost operation mode and 97 % in buck operation mode. The on-board charger developed by Radimov et al. is a bi-directional, three-stage, on-board charger with a peak efficiency of 96.65 % [43]. Schram et al. determined the V2G round-trip efficiency of a Renault Zoe with a bi-directional on-board charger to be 85.1 % and of a Nissan Leaf connected to an external charging station to be 87.0 % [44]. Due to the increasing demand for power electronic devices that are also used in EV powertrain systems researchers work on their improvements. One important improvement is the

development of wide-bandgap SiC and GaN based power semiconductor devices allowing enhanced performance and improved power density [45]. Dini and Saponara propose a model-based approach for the design of such bidirectional onboard charger electric vehicles [46]. For V2G services that require fast power provision, the delay of the power provision after the power set-point request is an important specification of the charging system. Furthermore, the difference between power request (set-point) and power output is of importance. These factors are often overlooked in literature but have been measured in previous research projects. In the Parker project, grid services were offered with a V2G setup using commercial DC-chargers and commercial EVs using CHAdeMO DC-charging. The researchers set power set-points and evaluated that the provided power by the charger lagged 7 s behind the requested power and the set-point error was 8.7 %. The maximum charger efficiency of the 10 kW chargers was 86 % and the efficiency exhibited a large drop at charging power below 20 % of the rated power [47]. Another project that investigated V2G services with EVs was the INEES project in Germany. In this project, experimental 10 kW DC charging stations were used with VW eUps that use a CCS plug system. The power set-point was reached almost instantaneously with this setup [48]. In the provision of power by a fleet of EVs it was observed that the power set-point for the fleet was reached within 1 s [49]. In conclusion, extensive literature exists about individual component models of an EV but especially the charging control model with the charger delay and power set-point accuracy is often overlooked. In this publication we specifically parameterize all components of an EV relevant to driving, charging and the provision of V2G services which lacks in literature.

2. Methodology

We parameterize and validate the EV model with the Smart electric drive (3rd Generation [50], production year and manufacturer: 2013, Daimler AG) shown in Figure 1a. The specifications of the Smart e.d. (3rd Generation) are summarized in Table 2. The model is implemented in Matlab[®]/Simulink.

Table 2. Specifications of Smart e.d. (3rd Generation) [51].

General Specifications	
Max. speed	125 km/h
Acceleration 0–100 km/h	11.5 s
Weight	900 kg
Traction Battery	
Chemistry	Li-Ion (NMC/Graphite)
Nominal Capacity	17.6 kWh
Rated/Max Voltage	339 V/391 V
Rated capacity	52 Ah
Layout	93s1p
Weight	179.6 kg
Permissible Temperature	−25–55 °C
Cooling	liquid cooling (water/glycol mixture)
Electric Motor	
Motor type	AC synchronous motor
Max. output	55 kW
Max. continuous output	35 kW
Peak Torque	130 Nm
Max. rpm	11,800
On-Board Charger	
Standard	IEC62196-2 & ISO 155118
Type	1-phase AC & 3-phase AC
Max. Power	22 kW

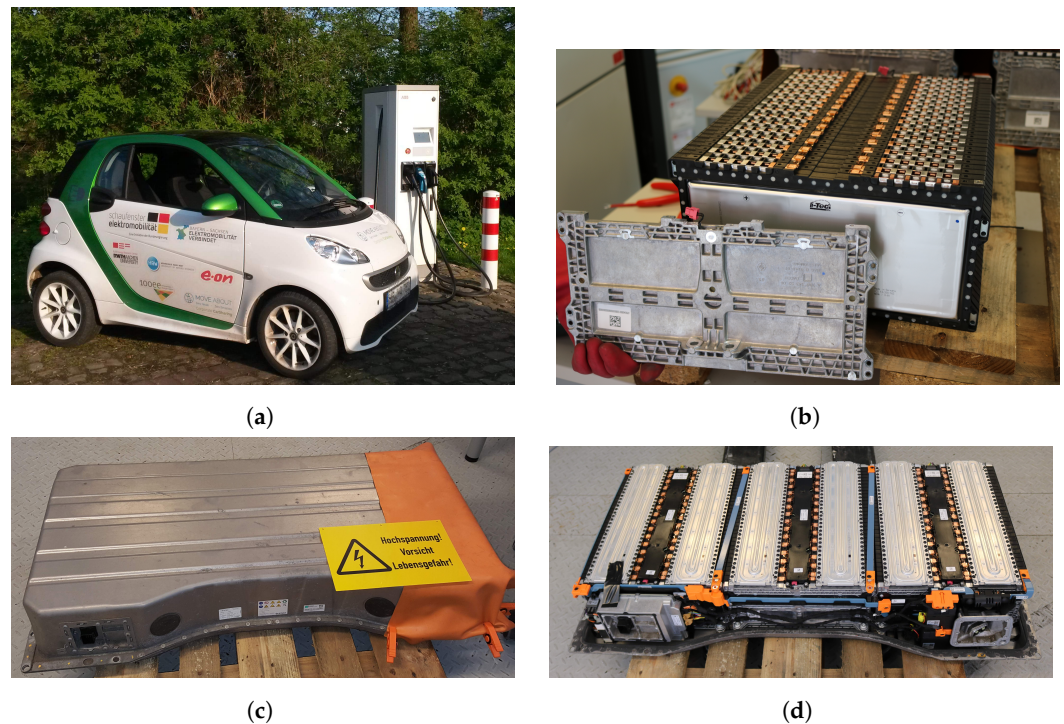


Figure 1. Pictures of the Smart e.d., its battery pack and a single battery pack module. (a) Smart e.d. (2013) in front of a charging station; (b) Single Module with outer plate taken off with a visible single cell of the 31 cells of the module; (c) Traction battery pack of Smart e.d.; (d) Traction battery pack of Smart e.d. without casing. 3 Modules with 31 cells each connected in series (93s1p) with liquid cooling plates and slave BMS. Bottom left: Master BMS. Bottom right: DC connector.

2.1. Electric Vehicle Model

The EV model is divided into several parts:

1. Traction battery model
 - (a) General (Section 2.1.1)
 - (b) Electrical model (Sections 2.1.2 and 3.1)
 - (c) Thermal model and traction battery pack materials, volume and weight distributions (Sections 2.1.3 and 3.2)
 - (d) Aging model (Sections 2.1.4 and 3.3)
2. BMS and charger model (Sections 2.2 and 3.5)
 - (a) Charger efficiency
 - (b) Charging control model

2.1.1. Traction Battery

The traction battery of the Smart electric drive (2013) is mounted at the bottom of the vehicle, has a battery layout of 93s1p and a capacity of 17.6 kWh. The battery management system (BMS) limits the the usable SOC range to 3.2–95.3%, which results in a usable battery capacity of 16.2 kWh. More specifications about the battery given by the official data sheet can be found in Table 2. The traction battery is housed in a case (see Figure 1c) that is constructed from a bottom part made of steel and a top part made of aluminum. The battery consists of three modules with 31 cells each that are all connected in series (see Figure 1b,d). In addition to the modules, the pack contains the Master BMS, the DC connector, HV contactors, shunt, precharge circuit, cooling system pipes and a desiccant cartridge.

Each module houses 31 cells which are held in place by plastic frames and are electrically connected via copper connectors. Two metal parts at each end and metal rods that go through the whole module provide stability. The slave BMS sits between the aluminum cooling plates on top of the module. The cooling plates cool (or heat) the terminals of

the cells which allows cooling (heating) within the cell. Between the copper conductor and the cooling plate, strips of thermal interface material (TIM) are placed such that the aluminum cooling plates do not short-circuit the cells. Within the cooling plates a coolant (water/glycol mixture) circulates in order to cool the battery pack during driving and charging. If the battery temperature falls below 0 °C the coolant is heated in order to ensure safe operation of the battery pack [51].

The battery cell is the HEA50 high energy cell (ICS 13/330/162, IMP 13/330/162) manufactured by Li-Tec (Daimler) with a nominal capacity of 52 Ah. The manufacturer also provides details about the aging characteristics of the cell in the data sheet (see Table 3). Cycle life time is given as 3000 cycles at 100% depth of discharge (DOD) and a charge/discharge rate of 2C/2C. The calendar lifetime is given as ≥ 5 years of shelf life at 50% SOC and -30 – 25 °C.

Table 3. Specifications of battery cell HEA50 high energy cell (ICS 13/330/162, IMP 13/330/162) of Smart e.d. (3rd Generation) [52].

Battery Cell Specifications:	
Name	HEA50 high energy cell
Type specification	ICS 13/330/162, IMP 13/330/162
Manufacturer	li-Tec (Daimler AG)
SOC operation limit	3.2–95.3 %
Nominal capacity	52 Ah (0.5 C discharge)
Nominal voltage	3.65 V
Voltage range	3.0–4.2V
Temperature range	-25 – 55 °C
Gravimetric energy density	147 Wh/kg
Volumetric energy density	280 Wh/L
Inner resistance	≤ 1.8 m Ω (5 s, 200 A, 50 % SOC)
Cathode	Li-Ion with LITARION [®] NMC (33% Ni, 33% Co, 33% Mn [53])
Anode	Graphite
Anode terminal	Copper
Cathode terminal	Aluminum
Separator	Ceramic (SEPARION [®])
Cell case material	PET
Width \times length \times depth	32.8 cm \times 16.1 cm \times 1.3 cm (50 % SOC)
Weight	1296.5 g

2.1.2. Electrical Model

The electrical model of the traction battery is based on the model of a single battery cell. Cell-to-cell variations within the pack in terms of capacity and inner resistance are neglected. Hence, also a balancing system is not required. This simplification leads to faster simulation times and is referred to in literature as a model on pack level in contrast to models on material or cell level [54].

In systems theory, classification of models are based on their physical interpretability. With this in mind, battery models can be divided into three categories: white box models, grey box models and black box models [55]. In this work a grey box model based on an equivalent circuit model (ECM) is used to model the electric behavior of the battery cell. A multitude of different ECMs is used in literature, such as in Ref. [56], which differ in their complexity, accuracy and required computational power. The ECM of choice in this work is shown in Figure 2 which is expected to provide a good trade-off between computational requirements and accuracy for the simulations. It consists of a voltage source, representing the OCV, in series with a resistance R_{ser} and two RC-elements. It is referred to in literature as a dual polarization model (Thevenin 2RC).

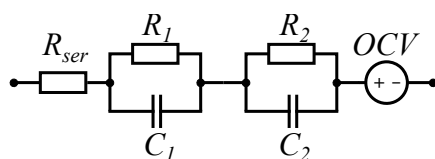


Figure 2. Equivalent circuit diagram of battery cell.

All parameters are dependent on the state of charge (SOC) and temperature of the cell. OCV measurements were carried out with a battery cell in a climate chamber while regulating the temperature. During the measurement the cell was discharged. For each SOC state the cell voltage was measured after a relaxation period (period with no load on the cell) such that the measured voltage can be regarded as the OCV. Additionally, two RC-elements and an ohmic resistance R_{ser} were parameterized in order to model physical processes occurring within the cell that have an impact on the electrical behavior. The resistance R_{ser} is the ohmic resistance due to limited conductivity for electrons and ions within the cell. It leads to instantaneous voltage drops when the cell is under load. The first RC element models the intercalation/de-intercalation of Li-Ions into/from the electrodes where R_1 models the charge transfer resistance and C_1 models the double layer capacity at the respective electrodes. The second RC element models the concentration gradient of Li-Ions and diffusion in the electrolyte [57–59].

The dynamic processes within the cell have different speeds. The overvoltage at a reaction surface with double layer capacitance builds up within milliseconds, the inhomogeneous electrolyte concentration reaches a steady state after one or several minutes and the solid state diffusion overvoltage builds up and decays even more slowly [53].

The resistance and capacity parameters of the equivalent circuit diagram for the cell were fitted with impedance spectroscopy measurements using a Digatron EIS-Meter in a frequency range of 1 mHz to 6 kHz and a temperature regulated climate chamber. Further information about impedance spectroscopy measurements with EIS-Meters can be found in the dissertation of Kiel [60]. Further information about extraction of ECM parameters and their interpretation with regards to physical processes within the cell can be found in the dissertation of Witzhausen [53]. Impedance spectra at different SOCs and temperatures of the cell were measured and the parameters were extracted from resulting Nyquist diagrams. The results are described in Section 3.1.

2.1.3. Thermal Model

The temperature of the battery pack has a direct influence on its electrical performance, capacity, efficiency and safety. During the operation of the battery pack, heat is produced. According to Bernardi et al. [61] the following equation describes the heat generation current \dot{Q} in a cell

$$\dot{Q}_{gen} = \dot{Q}_{irr} + \dot{Q}_{rev} + \dot{Q}_{react} + \dot{Q}_{mix}, \quad (1)$$

where

- \dot{Q}_{irr} is the irreversible ohmic heat generation,
- \dot{Q}_{rev} is the reversible heat generation due to the intercalation and deintercalation of ions at the electrodes,
- \dot{Q}_{react} is the heat generation due to side reactions of the electrolyte with the electrodes (i.e., phase changes) and
- \dot{Q}_{mix} is the heat generation associated to the relaxation of concentration profiles.

The heat currents \dot{Q}_{react} and \dot{Q}_{mix} are often neglected in literature in lithium-ion battery modeling [55]. In this model also only \dot{Q}_{rev} is not considered. This simplification can also be found in the work of Magnor [62]. In order to model reversible heat, the entropy coefficients of the cell would have to be determined. In theory, the parameterization of the entropy coefficients could be achieved with the measurement of the voltage response after a temperature change of the cell. A lumped thermal model is used in this publication as the

irreversible ohmic heat generation \dot{Q}_{irr} is dominant for large currents [63]. We deem this to be an acceptable simplification due to the scope of this research on large signal application.

The battery pack of the Smart e.d. is cooled during driving and charging by a liquid cooling system in contrast to other battery packs which are cooled by forced convection with the use of a Fan (i.e., Mitsubishi iMiEV) or free convection (i.e., VW eUp). Furthermore, privately owned vehicles only spend less than 4% of their time driving (own analysis with data of [64] in Germany). The use of a simplified reduced order model is therefore assumed to be sufficient to account for the impact of temperature on performance and aging of the battery pack.

The equivalent circuit model for the reduced order model is shown in Figure 3.

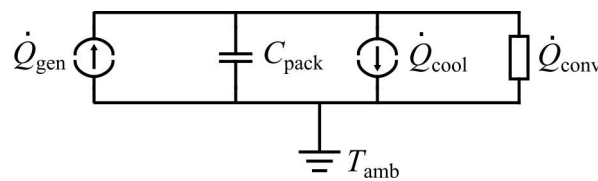


Figure 3. Equivalent circuit model of the thermal model of the battery pack.

The thermal model equation is then

$$C_{pack} \cdot \frac{dT_{pack}}{dt} = \dot{Q}_{gen} - \dot{Q}_{diss}, \quad (2)$$

with

$$C_{pack} = m_{pack} \cdot C_{pack-spec}. \quad (3)$$

Here, C_{pack} is the specific heat capacity of the battery pack, m_{pack} is the battery pack mass, \dot{Q}_{gen} and \dot{Q}_{diss} are the heat generation rate and heat dissipation rate respectively. The dissipation rate \dot{Q}_{diss} is separated into two components

$$\dot{Q}_{diss} = \dot{Q}_{cool} + \dot{Q}_{conv}, \quad (4)$$

where \dot{Q}_{conv} is the cooling rate due to the heat transfer to the surroundings by convection and \dot{Q}_{cool} is the cooling/heating rate due to the the liquid cooling system. The convection rate is calculated as

$$\dot{Q}_{conv} = (\alpha_x + \alpha_y + \alpha_z) \cdot \Delta T \quad (5)$$

with $\Delta T = T_{pack} - T_{ambient}$ and α being the convection coefficient in one spatial direction:

$$\alpha = \alpha_{spec} \cdot A \quad (6)$$

A is the surface area and α_{spec} is the specific heat transfer coefficient. Literature values for α_{spec} relevant for this study are shown in Table 4

The cooling system of the drive train components cools the traction battery, charger, engine, power electronics control unit and motor. It consists of two coolant pumps, traction battery heater, chiller, electric expansion valve and an electromotive water valve. The coolant is a glycol/water (50:50) mixture. The BMS can also decouple the coolant circuit of the traction battery from the rest of the cooling circuit via the electromotive water valve if the traction battery needs specific cooling [51].

The calculation of the flow rate and cooling power of the liquid cooling system is based on the model done by Cédric [65]. The flow rate depends linearly on the battery temperature and the coolant temperature is assumed to be equal to the ambient temperature. The cooling power provided by the liquid cooling system is

$$\dot{Q}_{cool} = \Delta T \cdot \rho_{coolant} \cdot c_{coolant} \cdot v_{coolant}, \quad (7)$$

with the density $\rho_{coolant} = 1080 \text{ kg/m}^3$, specific heat capacity $c_{coolant} = 3320 \text{ J kg}^{-1} \text{ K}^{-1}$ and

$$v_{coolant} = \left| \frac{T_{pack}}{45} \cdot 1.513 \times 10^{-5} \text{ m}^3 / (\text{s}^\circ\text{C}) \right| \quad (8)$$

which is devised from information found in [65].

At low temperatures the inner resistance of the battery increases due to, among other effects, lower ion conductivity of the electrolyte. When charging a lithium-ion battery at low temperatures, high surface area lithium deposition on the graphite anode, also known as plating, can occur, which is a safety issue due to short-circuit risks [66].

Therefore, during the charging process the coolant is heated when the battery temperature falls below 0°C [51]. To take this into account, during charging, the temperature of the battery pack is kept above 0°C in the model.

Table 4. Literature values for specific heat capacity.

Material	Specific Heat Capacity in kJ/(kg K)
Cell	1095 [67]
Steel	502 [68]
Aluminum	891 [69]
Plastic (PP)	1570 [70]
Air	1.01 [67]

2.1.4. Aging Tests

In order to account for the aging of the EV battery cell we evaluated accelerated aging tests of Li-Tec HEA40 cells. These cells are identical in composition and construction to the Li-Tec HEA50 cells apart from the capacity and dimensions. Therefore, the results are transferable to the Li-Tec HEA50 cell of the Smart e.d. (3rd Generation).

The aging process of a battery cell leads to a reduction in capacity and an increase of its inner resistance. Calendar and cycle aging were considered separately. This approach and the parameterization process is described in detail by Schmalstieg in [19]. The aging behavior of the Li-Tec HEA40 cell was tested in accelerated aging tests in the laboratory at the institute for power electronics and electrical drives (ISEA) at RWTH Aachen. In order to separately measure the effects of calendar and cycle aging factors, two separate test procedures were carried out. The test conditions are shown in Figure 4a,b. Periodically, every 30–50 days, each cell underwent a checkup. During a checkup the capacity of the cell was measured in a 1C discharge and the inner resistance was evaluated from the voltage response of the cell to a 1C current charge pulse after 10 s. The overall aging of the cell is given by the superposition of calendar and cycle aging.

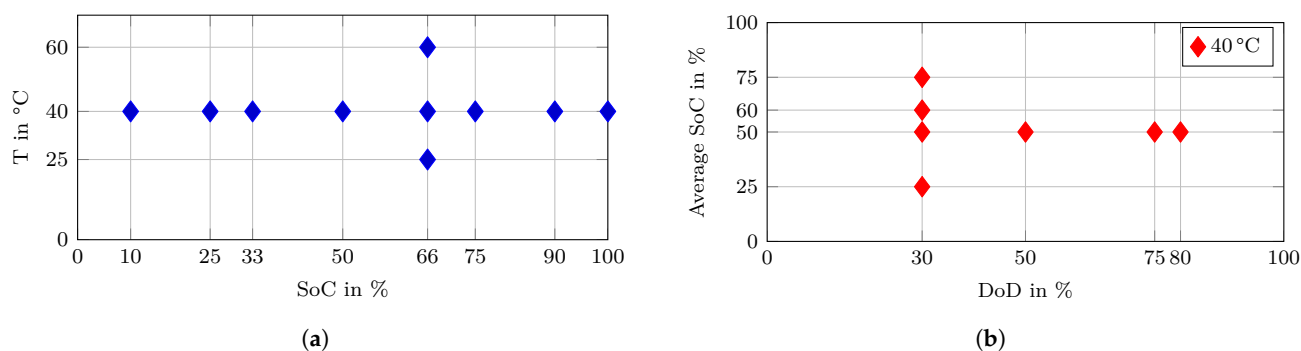


Figure 4. Accelerated aging test conditions. (a) Calendar aging test conditions at different SOC levels and temperatures; (b) Cycle aging test conditions at different average SOC levels and DoDs. All cycle aging tests were carried out at 40°C .

Calendar Aging

Calendar aging occurs at all times during storage and operation. In the calendar aging test the battery cells were stored in climate chambers at a constant cell temperature and cell voltage. The test conditions for calendar aging are shown in Figure 4a. Three cells were tested for each test condition and their performance was averaged.

Cycle Aging

In contrast to calendar aging, cycle aging occurs only when the cell is charged and discharged (cycled). During cycling the intercalation and de-intercalation of lithium ions leads to volume changes of the electrode material. This in turn can lead to crack-and-repair of the solid-electrolyte-interface (SEI) that consumes lithium (capacity loss) and increases its inner resistance. Furthermore active material particles can loose contact to the electrode (capacity loss) [19].

During the cycle aging test the battery cells were cycled (charged and discharged) with a current of 1C (50 A) and the cell temperature was kept constant at a temperature of 40 °C in a climate chamber. The test conditions are shown in Figure 4b. One cell was tested for each condition. During the cycle aging tests also calendaric aging occurs which has to be accounted for during the fitting process.

2.2. Charger and BMS Charge Control

In Figure 5 the laboratory setup for the parameterization of the charger and the controller for the charging process is shown. Two measurement points were used. At measurement point 1 the battery voltage and the battery current were measured. For this measurement the internal measurement devices of the vehicle were used which broadcast the values via the CAN-Bus. Via a CAN-Bus interface, the communication and therefore the measurement values were recorded. Measurement 2 was carried out on the grid side with a smart meter. The EV has an in-built 3-phase AC charger with a maximum charging power of 22 kW. The wallbox in the test setup has a Type 2 socket at which EVs can be charged via Mode 3 of IEC 61851-1. The maximum rated charging power is 11 kW (16 A, 3-phase). The supply equipment communication controller (SECC) of the wallbox was controlled and monitored via a Modbus-TCP interface. Via this interface the maximum current can be set which the SECC transmits to the EV via pulse-width modulation (PWM) in accordance to IEC 61851-1. The SECC that was used, was only able to set integer values for the maximum charging current. Therefore, the charging current could only be increased/decreased in 1 A steps starting at a minimal current of 6 A.

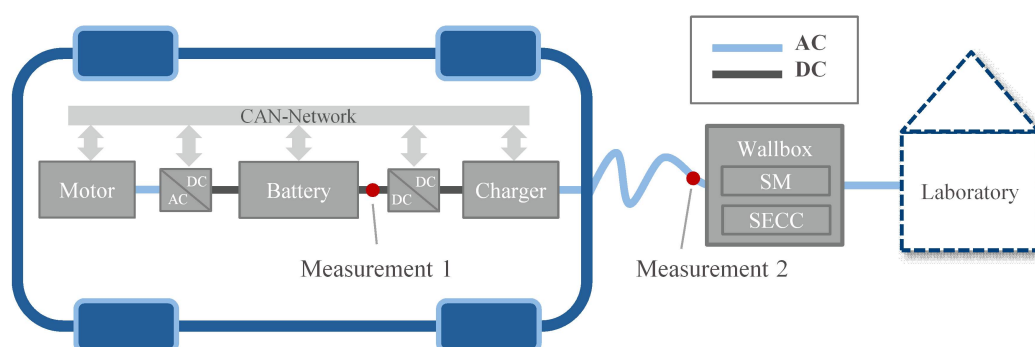


Figure 5. Laboratory setup for charger efficiency measurement

As it was not possible to switch from 3-phase to 1-phase charging mode via the SECC for the Smart e.d., the measurements for 1-phase charging were carried out with the emergency charging cable of the Smart e.d. without the use of the wallbox. The emergency charging cable plugs into a Schuko (protective contact) socket and enables 1-phase charging via Mode 2. The charging current is set by an in-cable communication controller. The con-

troller has two settings which set two different charging power settings: 1.8 kW and 2.9 kW. The possible set-points for the charging process in the laboratory are summarized in Table 5.

Table 5. Charging power setpoints for a grid voltage of 230 V and the Smart e.d. of the wallbox (3-phase charging) and the emergency charging cable (1-phase charging).

Charging Mode	Possible Setpoints
1-phase charging	1.8 kW and 2.9 kW
3-phase charging	4.1 – 11 kW in 690 W steps

3. Results

In this section we show the results of the EV model parameterization.

3.1. Electrical Model Parameters

Impedance spectra at different SOCs and temperatures of the cell were measured and the parameters for the ECM (see Figure 2) were extracted from resulting Nyquist diagrams. Furthermore, OCV measurements of the battery cell were conducted at different cell temperatures. The results are shown in Figure 6. Resistance R_{ser} shows little dependency of the SOC which indicates that no transient polarization process is occurring. Furthermore, R_{ser} varies approximately half an order of magnitude with the cell temperature. The increased resistance at higher temperatures correlates with the underlying chemical process of an increased reaction rate. This behavior is also visible for R_1 and R_2 and proves the physical interpretability of these parameters. Besides the resistances other important parameters to evaluate the parameterization of the ECM and the correspondence with physical processes are the time constants τ_1 and τ_2 of the RC elements. In our model, the time constants τ_1 and τ_2 model the duration of the reaction and balancing processes, respectively. Thus the following has to apply:

$$\tau_1 = R_1 \cdot C_1 < R_2 \cdot C_2 = \tau_2 \quad (9)$$

The results show the time constant τ_1 to be in the range of 10^{-2} s to 10^{-1} s while τ_2 in the 10^1 s to 10^2 s range. This is in accordance to the previously discussed physical interpretation and inequality (9). For the simulation of charging and discharging processes (V2G) with the simulation mode these time constants fit the dynamic processes. Impedance components in the ECM with smaller time constants are not necessary. The ECM and parameterization is therefore appropriate for prosumer household simulations and V2G applications.

3.2. Thermal Model Parameters

We disassembled a battery pack of the Smart e.d. and measured its dimensions (see Table 6). We also determined the weight and volume distributions of the pack and a single module (see Figure 7)). This was done by the disassembly of a Smart e.d. battery pack in the laboratory. In addition to the cells the modules and pack are made up of active and passive components. Active components are components that enable the functionality of pack such as the cooling system, BMS system and electrical connectors. The passive components are the housing components such as plastic frames between cells, metal binders, screws and the pack enclosure. Even though the Smart e.d. battery pack is highly compact, free air space makes up 47.46% of the pack volume. Due to the active and passive components and free air space the gravimetric and volumetric energy densities at pack level are considerably lower than on cell level. The gravimetric and volumetric energy densities on pack level are 98.3 Wh/kg (33.13% lower than on cell level) and 184.3 Wh/L (34.18% lower than on cell level) respectively.

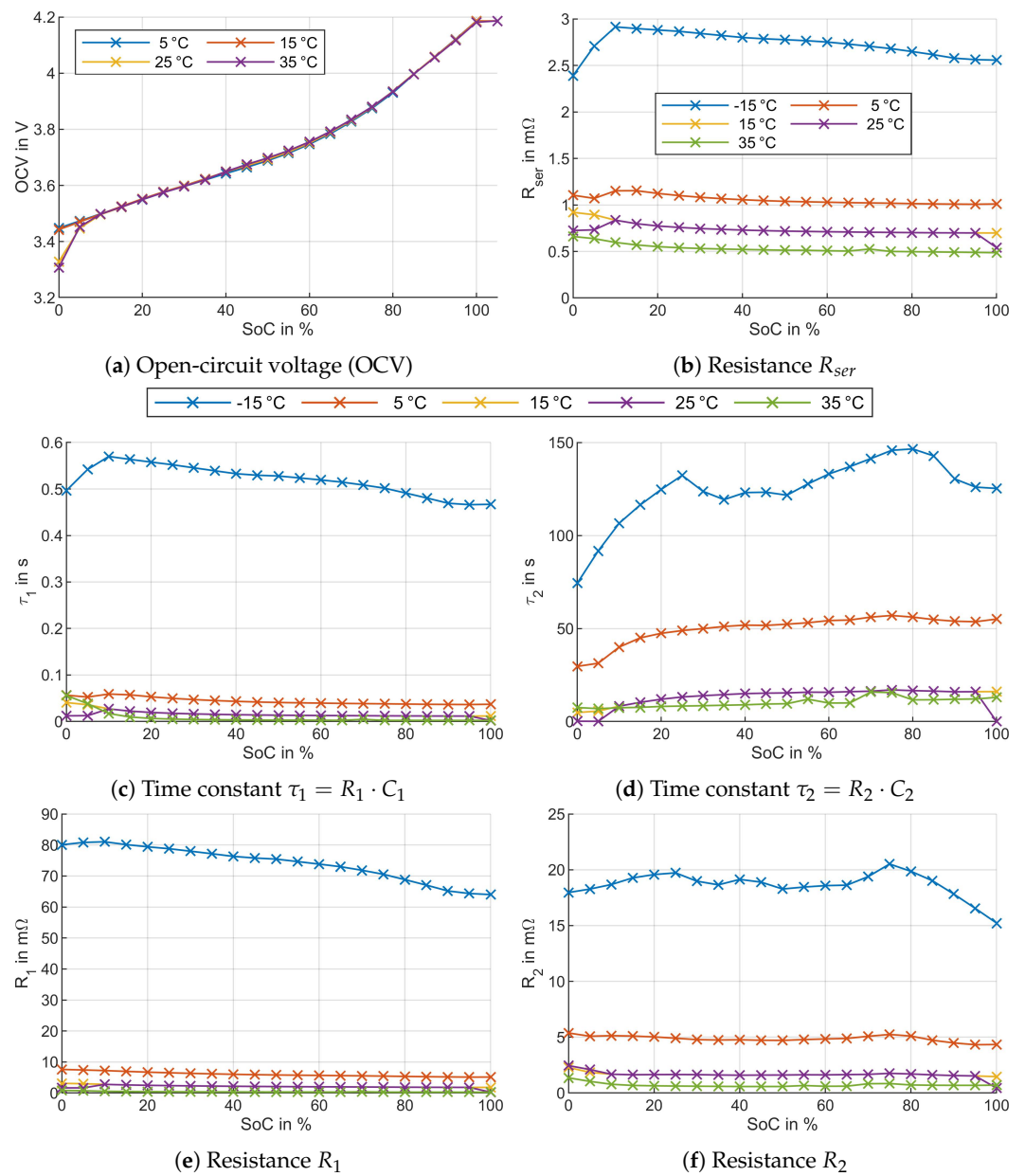


Figure 6. Electrical parameters of Li-Tec 52 Ah LiNiMnCoO₂ pouch cell.

Table 6. Traction battery pack and module dimensions.

Parameter	Pack	Modules with Slave BMS
Volume in L	95.86	74.5
Mass in kg	179.6	146.5
Surface area in m ²	1.69	1.36

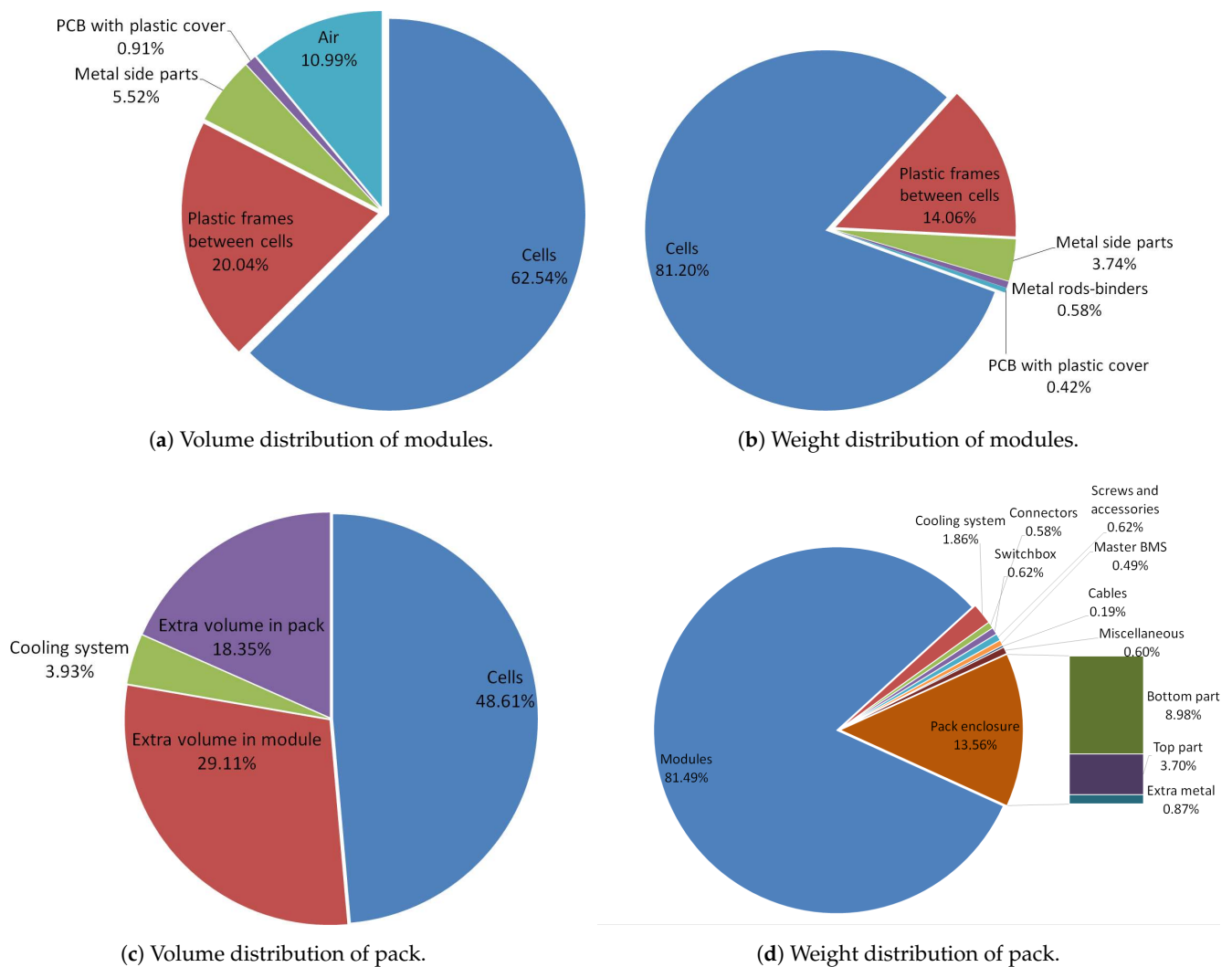


Figure 7. Volume and weight distributions of the Smart e.d. battery pack.

We calculate the thermal parameters for the thermal equivalent circuit diagram (shown in Figure 3) using literature values for the specific heat capacity (shown in Table 4) and the pack dimensions and weight distributions shown in Table 6. Different materials have different specific heat transfer coefficients to air and the battery pack is made up of different materials. Therefore, we fit the specific heat transfer coefficient for the open pack by performing simulations of the cooling phase of the pack without load after the 1C discharge measurement in the laboratory. The resulting specific heat transfer coefficient that provided the best agreement between simulation and data was $\alpha_{spec} = 5 \text{ W/m}^2/\text{K}$. As the battery pack was not mounted in the car during the pack tests in the laboratory we obtain different heat transfer coefficients sets for the EV operation tests. The resulting parameters are shown in Table 7.

Table 7. Values for heat capacity of the pack C_{pack} and the convective heat transfer coefficients α for each spatial direction (x,y,z) . Parameters of thermal battery pack model shown in Figure 3.

Parameter	EV Operation	Lab Pack Test
C_{pack} in kJ/K	17.12	17.12
α_x in W/K	0.726	0.472
α_y in W/K	3.470	2.863
α_z in W/K	1.383	0.899

3.3. Aging Model Parameters

We analyzed the aging of the battery cells in accelerated aging tests and fitted aging functions to the data.

3.3.1. Calendar Aging

The experimental data of the calendar aging test together with the time fit is shown in Figure 8a,b for the normalized capacity and in Figure 9a,b for the normalized resistance of the cell. As the cells age, their capacity decreases and their resistance increases. For each set point we tested three cells. The figures show that the aging characteristic of three cells at the same set point can differ to a large extent. In a previous study this was linked to variances of material properties and process parameters in the production process [71]. In order to fit the time dependence for calendar aging we averaged the experimental results for each set point and fit Equations (10) and (11) for capacity and resistance respectively:

$$C_{norm} = 1 - \alpha_C \cdot t \quad (10)$$

$$R_{norm} = 1 + \alpha_R \cdot t, \quad (11)$$

with capacity and resistance given as normalized parameters:

$$C_{norm} = \frac{C}{C_0} \quad (12)$$

$$R_{norm} = \frac{R}{R_0}, \quad (13)$$

where C_0 is the initial capacity and R_0 is the initial inner resistance.

Other exponents for the time dependency can be found in literature, such as 0.75, which was found to describe the time dependence for calendar aging in [19]. In [36], Ecker et al. used a square root time dependency for the fit which was motivated by the assumption of solid electrolyte interface on the negative electrode as the dominating aging factor. However, the authors observed a linear trend, especially at low SOC. In this work the linear approach yielded the best fit overall and was therefore chosen for this cell. The coefficients α_C are shown in Figure 8c,d. The coefficients α_R are shown in Figure 9c,d.

The results for calendar aging at 40 °C show accelerated loss of capacity of cells stored at higher SOC with a plateau between 50% and 75%. The results for the cell resistance show a plateau for cells stored between 25% and 75% SOC. The capacity of cells stored at 100% SOC decreases at a 250% higher rate than the capacity of cells stored at 90%. In turn the capacity of cells stored at 90% decreases at a 202% higher rate than the capacity of cells stored at 75% SOC. The highest rate of increase of the inner resistance exhibited cells stored at 90% and 100% SOC (see Figure 9a). However, the cell resistance never reached the end-of-life criterion of a 100% increase of the inner resistance. Figures 8b and 9b show the calendar aging test results for cells stored at 66% SOC and different temperatures. The aging rate of the cell depends strongly on the cell temperature. The rate of capacity decrease at an SOC of 66% is 617% higher at 60 °C than at 40 °C which in turn leads to a 655% higher rate than for cells stored at 25 °C. The results follow the same trend for the inner resistance. The cells stored at 60 °C and 66% SOC reached the end-of-life criterion of the inner resistance first after 200 to 300 days. In conclusion, avoidance of high cell temperatures (<60 °C) and high storage SOC (>75%) is highly beneficial to reduce calendar aging of this cell. These results are in accordance with other studies in which lithium ion cells generally showed accelerated aging at higher SOC and temperatures [19,72,73]. The fit of the SOC and temperature dependence of the linear coefficient α_C is beyond the scope of this paper.

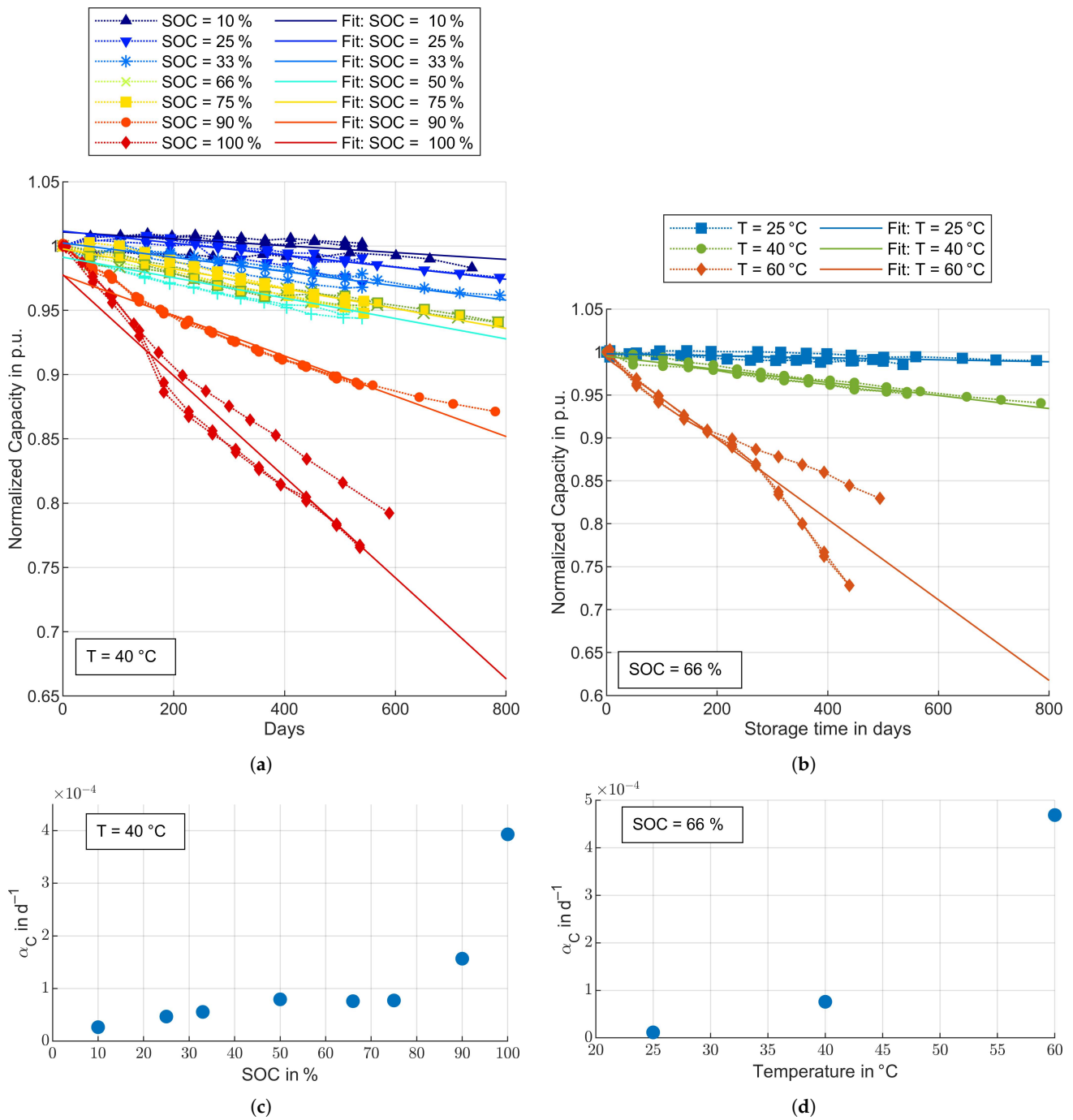


Figure 8. Capacity test and time fit results for cell capacity in calendar aging tests. (a) Capacity test and time fit results for cells stored at $40\text{ }^{\circ}\text{C}$ in the calendar aging tests; (b) Capacity test and time fit results for cells stored at 66% SOC in the calendar aging tests; (c) Linear coefficient α_C of the time fit results for cells stored at $40\text{ }^{\circ}\text{C}$ in the calendar aging tests; (d) Linear coefficient α_C of the time fit results for cells stored at 66% SOC in the calendar aging tests.

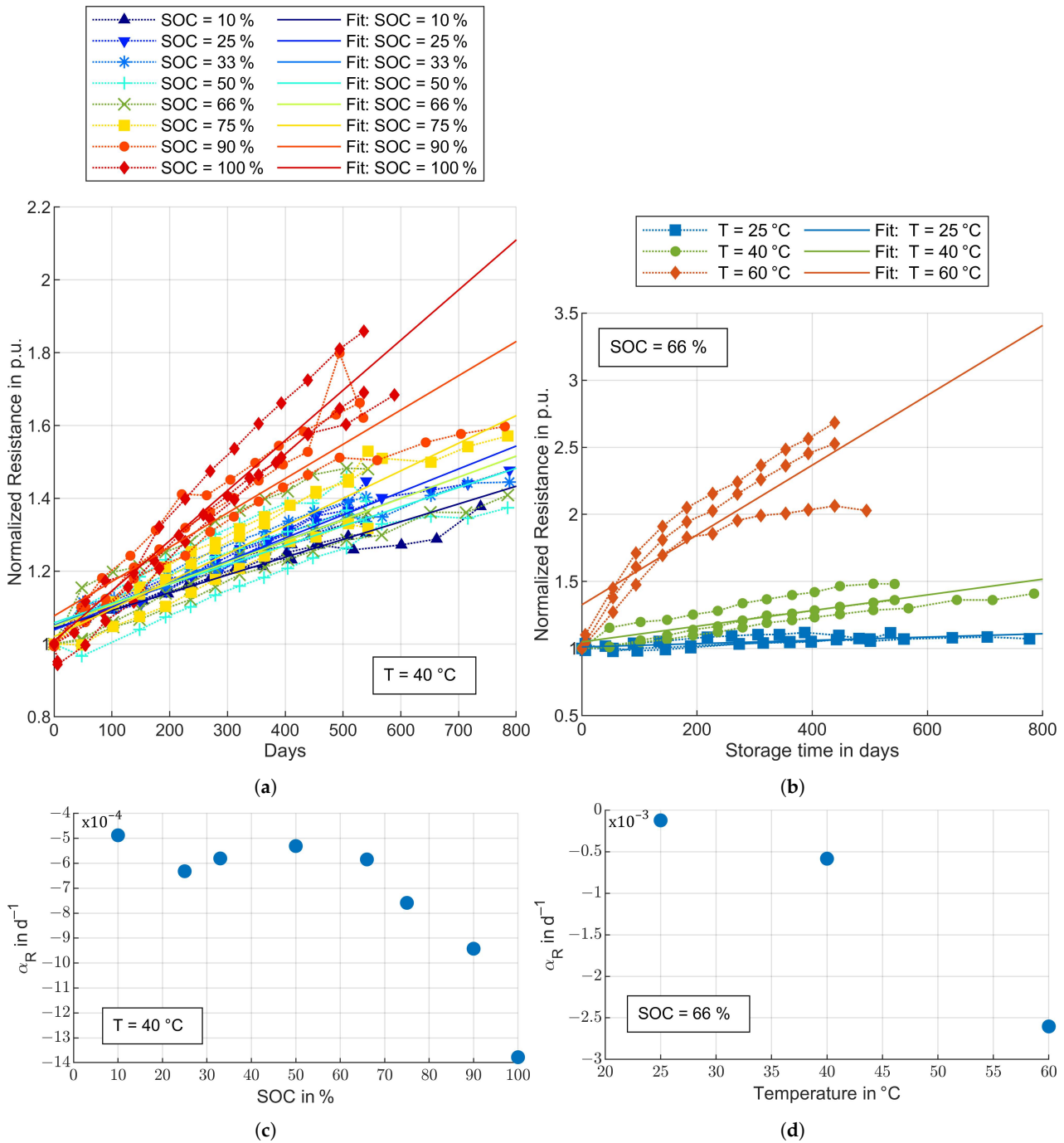


Figure 9. Capacity test and time fit results for inner cell resistance in the calendar aging tests. (a) Inner resistance measurement and time fit results for cells stored at $40\text{ }^{\circ}\text{C}$ in the calendar aging tests; (b) Inner resistance measurement and time fit results for cells stored at 66% SOC in the calendar aging tests; (c) Linear coefficient α_R of the time fit results for cells stored at $40\text{ }^{\circ}\text{C}$ in the calendar aging tests; (d) Linear coefficient α_R of the time fit results for cells stored at 66% SOC in the calendar aging tests.

3.3.2. Cycle Aging

The results of the cycle life tests are shown in Figures 10a,b for the capacity and Figures 10c,d for the inner resistance. All tests were carried out at $40\text{ }^{\circ}\text{C}$. The cells in the cycle life tests age due to calendar aging and cycle aging. The results of tests carried out with different DOD show that the lifetime of the cells decrease with increasing DOD. All cells reached at least one of the two end-of-life criteria (80% of initial capacity and 200% of

initial inner resistance) with the exception of the cells cycled with a DOD of 30% around a mean SOC of 60% and 75%. The first cell to reach EOL was the cell that was cycled with a DOD of 95% around a mean SOC of 50%. The EOL was reached in the EQFC range of 2649 to 2849. The second cell to reach EOL is the cell that was cycled with 80% DOD around an SOC of 50%. The EOL is reached after 3634 EQFC.

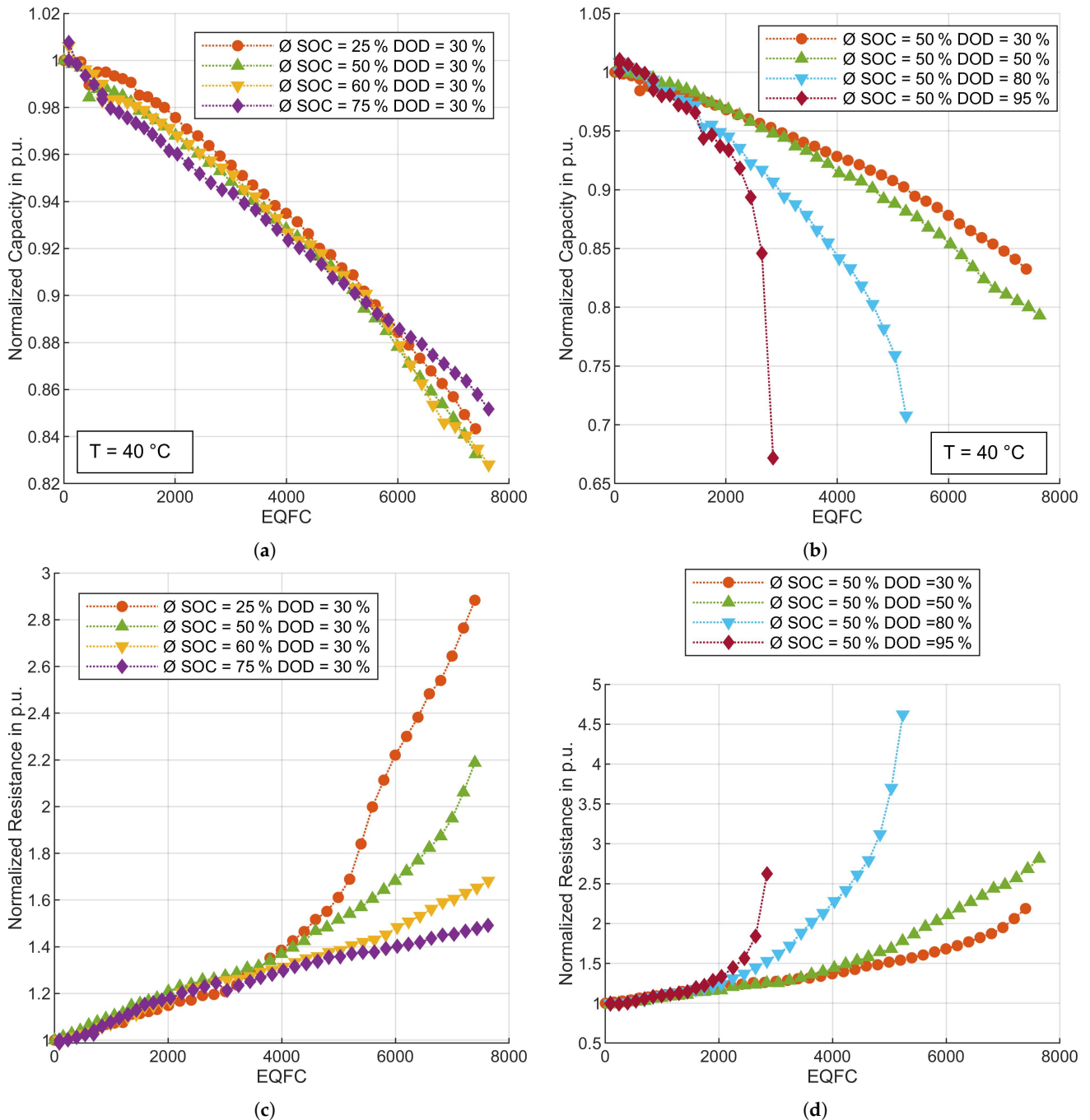


Figure 10. Capacity test results for cycle aging tests. (a) Capacity test results for cells cycled with 30% in the cyclic aging tests ($T = 40\text{ }^{\circ}\text{C}$); (b) Capacity test results for cells cycled around 50% in the cyclic aging tests ($T = 40\text{ }^{\circ}\text{C}$); (c) Inner resistance measurement results for cells cycled with 30% in the cyclic aging tests ($T = 40\text{ }^{\circ}\text{C}$); (d) Inner resistance measurement results for cells cycled around 50% in the cyclic aging tests ($T = 40\text{ }^{\circ}\text{C}$).

3.4. Validation of Traction Battery Model

In the research project GoELK several Smart e.d. were operated in commercial fleets. After approximately two years of operation in a fleet for geriatric care, the battery packs of two Smarts were tested and disassembled in the laboratory at ISEA (RWTH Aachen). The battery pack was removed from the EV, the lid was taken off the battery pack and the pack was connected to a Digatron Pack Test unit. During the operation of the pack using the Digatron Pack Test unit, the BMS and the liquid cooling system of the Smart were not activated. The pack voltage, each cell voltage, ambient temperature and cell temperatures were recorded. In Figure 11a,b, the measurement of a full discharge and charge test respectively are shown and compared to the model simulation results. As the lid had been removed and the liquid cooling system was not activated, the thermal model was parameterized with the values for “Lab Pack Test” in Table 7. In Figure 11c,d, the measurement and simulation of a driving profile and a charge process with 11 kW is shown. For these simulations the thermal model was parameterized with the values for *EV Operation* in Table 7 for a normally operated EV (Smart e.d.).

In Table 8 the profile characteristic and the deviation between measurement and simulation are shown for the four profiles. Overall, the comparison between measurement and simulation shows good agreement. It should be noted that in the model the possible deviation in voltage, state of charge and state of health between the 93 cells is neglected. Especially in the case of the laboratory pack test measurements this could have a non negligible effect as the BMS, and therefore also cell balancing, is not operational. The RMSE per cell (93s1p configuration) between measurement and simulation is between 18.49 mV and 31.26 mV for the profiles with a low dynamic (charging and constant current profiles). The RMSE per cell for the driving profile was higher with 67.17 mV, which is still sufficiently accurate. Furthermore, this was expected as the ECM of the battery cell was parameterized to show higher accuracy for long profiles with low dynamics as the EV spends longer times charging than driving in the prosumer simulations. The accuracy of the model is comparable to previous studies on battery cell and pack modeling. Li et al. achieved a RMSE of 70 mV per cell in a 0.5C charge of a battery pack. However, no dynamic drive cycle was tested in this study [11]. Studies that model single cells achieve more accurate results as the effect of cell variations within a pack is not present. Zhu et al. reached a lower RMSE of 8.61 mV under the urban dynamometer driving schedule (UDSS) for a single cell. Schmid et al. reached a similar RMSE of 5.74 mV to 12.32 mV for single cells in a battery pack with a profile based on the WLTP driving cycle and battery fault introduction [12]. In case of the pack temperature, the errors in the lab test however, showed acceptable accuracy with maximum absolute errors of 1.05 K and 1.99 K for the 1C discharge and 1C charge respectively. The errors are comparable to the results of Mesbahi et al. who reached a maximum error of 1.35 K with the use of distributed equivalent thermal circuit modeling of a 40 Ah NMC pouch cell [10]. The impact of inaccuracies of the thermal model during operation are also limited as a privately used vehicle in Germany is parked for 97% of the time [4]. The simulation time for the model is 17 s for a slow charge profile of 12 h with Simulink 2020a on a standard laptop with an Intel Core i7-6820HQ (2.7 GHz) without parallelization.

In summary, the simulation model yields accurate results for the operation of an EV in prosumer households.

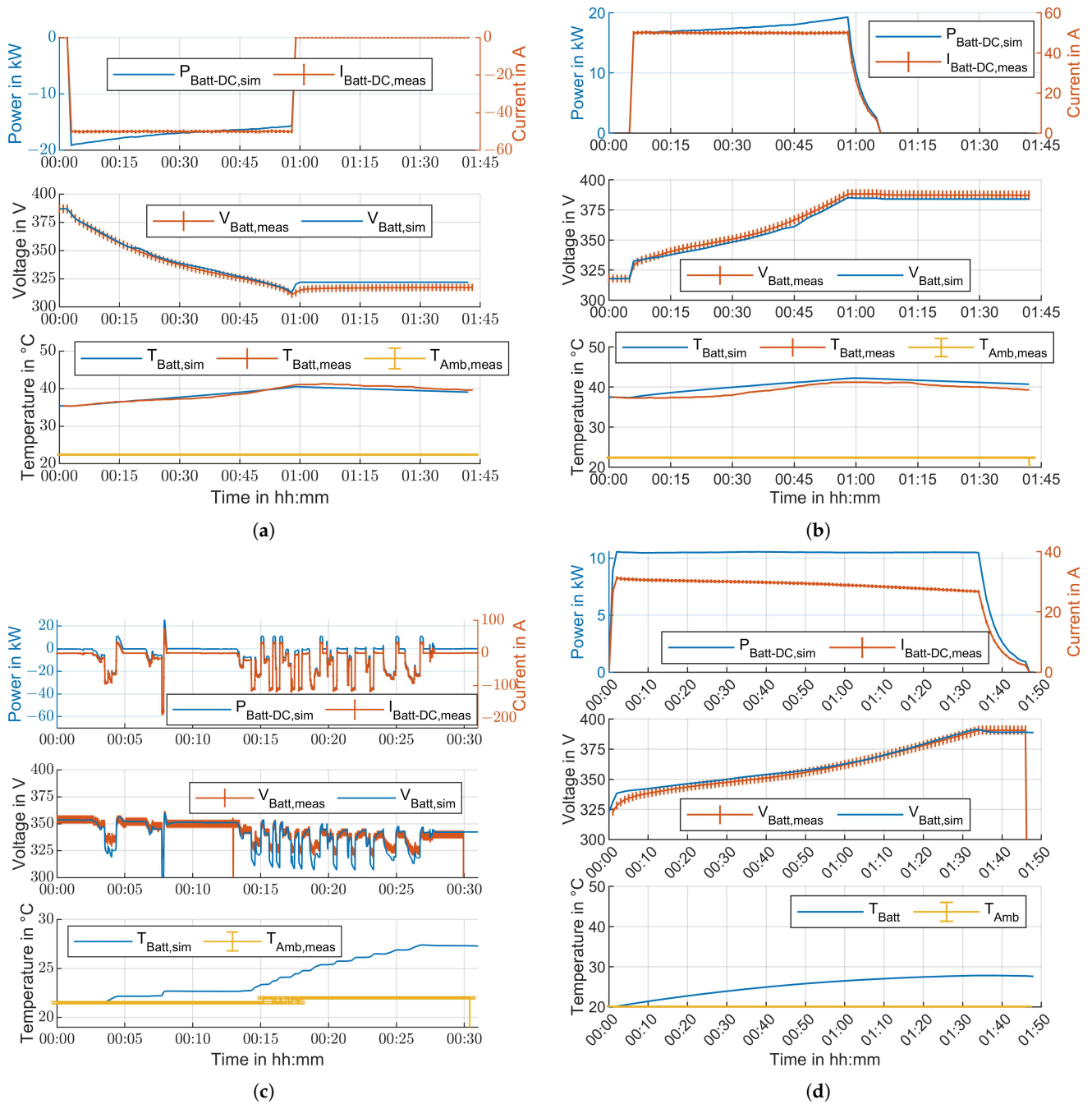


Figure 11. Validation of battery model using laboratory and field test data. (a) Laboratory pack test measurements and simulation: Full 1C Discharge; (b) Laboratory pack test measurements and simulation: Full 1C Charge; (c) Driving profile measurement and simulation with 1 s resolution; (d) Measurement and simulation of 11 kW charge.

Table 8. Summary of validation profile parameters and simulation deviations.

	Laboratory Pack Test		EV Operation	
Profile parameters:				
Profile	1C Discharge	1C Charge	Driving	Charge (11 kW)
Figure	Figure 11a	Figure 11b	Figure 11c	Figure 11d
Charge in Ah	-46.46 ± 0.47	46.54 ± 0.47	-10.34 ± 0.10	47.16 ± 0.47
Energy in kWh	-15.87 ± 0.32	16.60 ± 0.33	-3.41 ± 0.07	16.9 ± 0.34
Duration in min	55.95	60.78	29.88	105
Cell voltage deviation:				
RMSE in mV	18.49	31.26	67.17	30.22
Max. abs. error in mV	80.92	59.45	278.87	43.59
Pack temperature deviation:				
RMSE in K	0.36	1.29	n.a.	n.a.
Max. abs. error in K	1.05	1.99	n.a.	n.a.

3.5. Charger

In this section, we present the results of the charger efficiency and charge control parameterization.

3.5.1. Charger Efficiency

In Figure 12a, the DC current of the traction battery at measurement point 1 (see Figure 5) is shown versus the SOC during charging processes. The power values denote the maximum power that was reached during the charging process. The curves for 1.8 kW and 2.9 kW were carried out with 1-phase whereas the other measurements were carried out with 3-phases. As the EV charges with constant power until the voltage limit is reached, the battery current decreases with increasing SOC. The sharp drop of the battery current at high SOC values is due to the constant voltage (CV) phase upon reaching the voltage limit. In Figure 12b, the efficiency of the charging process between AC power output of wallbox and DC power of battery (measurement points 2 and 1 respectively in Figure 5) is shown versus the battery voltage for the same charging processes. The battery voltage is in the range of 318.1 V–391.8 V for these measurements. The efficiency of the charger increases with the charging power. The efficiency for one full charge ranges from 73% for 1-phase charging with a setting of 1.8 kW to 92% for 3-phase charging with a setting of 11 kW. The lower values for the efficiency at low and high values of the battery voltage are due to low charging powers during the ramp up at the beginning of the charging process and the ramp down during the CV phase respectively.

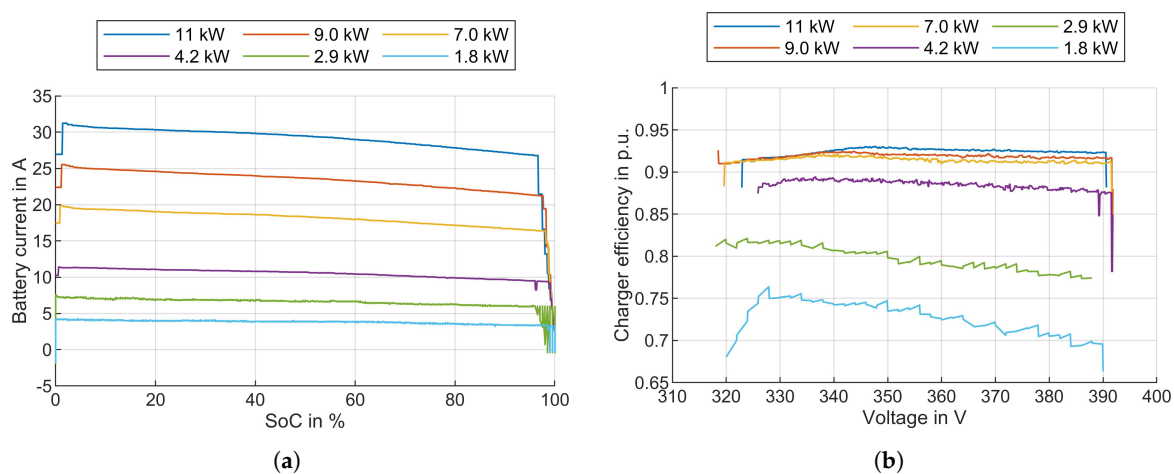


Figure 12. Measurement results of EV charging. (a) Charging current (DC) versus SOC using different charging power settings; (b) Charging efficiency versus battery voltage using different charging power settings.

3.5.2. Charge Control

When the setting of the maximum charging current is changed via the CP, the new charging current is not reached by the EV immediately, but with a delay. This behavior is shown in Figure 13 for the Smart. In Figure 13a, the charging power on the AC side of the wallbox is shown after a new maximum current setting has been communicated to the EV via the CP at time $t = 0$ s. The new power set-point $P_{EV,EMS}$ is not reached immediately but it takes some time for the power to ramp up. In all measurements the power set-point was reached after at most 52 s. The ramp up follows a similar curve for all measurements. Only in the case that the initial power set-point of the EV was 0 W, we observed an initial reaction delay in the order of seconds. We illustrate the similar behaviour of the EV upon a new power set-point with the normalized power P_{norm} in Figure 13b. We calculated it as follows:

$$P_{norm} = \frac{(P(t) - P(t = 0))}{P_{diff}} \quad (14)$$

$$P_{diff} = P_{EV,EMS} - P(t = 0) \quad (15)$$

In order to model the delay in the simulation we parameterize the average ramp up behavior P_{ramp+} using the average of all measurements $P_{norm,mean}(t)$ shown in Figure 13b. We model the ramp up for a requested power increase according to Equation (16), where t denotes the time after the the new power set point has been set.

$$P_{ramp+}(t) = \begin{cases} P(t = 0) + P_{diff} \cdot P_{norm,mean}(t) & 0 \leq t \leq 52 \text{ s} \\ P_{EV,EMS} & t \geq 52 \text{ s} \end{cases} \quad (16)$$

The ramp down time until a lower power set point is reached is shorter with 4 s on average. We model the ramp down for a requested power decrease according to Equation (17), where t denotes the time after the the new power set point has been set.

$$P_{ramp-}(t) = \begin{cases} P(t = 0) & 0 \leq t \leq 4 \text{ s} \\ P_{EV,EMS} & t \geq 4 \text{ s} \end{cases} \quad (17)$$

In Figure A1 a measurement of a charging process of the EV is shown with the requested charging power by the EMS and the actual charging power of the EV.

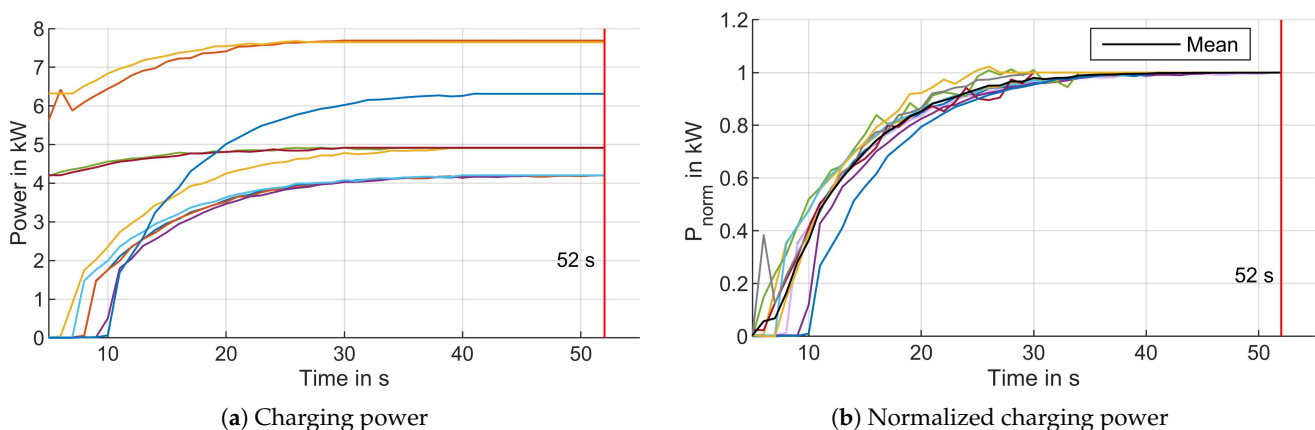


Figure 13. Charging power (AC, measurement point 2) after a new maximum current setting is communicated to the EV via the CP at time $t = 0$ s. Each colored line is one measurement and in (b) the black line illustrates the mean of all normalized charging power measurements. After 52 s the new charging power setting is reached by the EV.

4. Conclusions

In this publication, we parameterized a comprehensive EV simulation model. We parameterized a model for the traction battery, charger and charging process control via an EMS system for the Smart e.d. (2013). The electrical model of the battery cell (50 Ah, manufactured by li-tec (Daimler AG)) is based on an equivalent circuit diagram (Figure 2) with a serial resistance, two RC circuits and a voltage source (dual polarization Thevenin model). It was parameterized via capacity tests, OCV measurements, pulse tests and impedance spectroscopy tests. The two time constants τ_1 and τ_2 of the electrical model are in the range of 10^{-2} s to 10^{-1} s and 10^1 s to 10^2 s range respectively. The electrical model of the battery cell was scaled to obtain the electrical model of the traction battery pack (17.6 kWh, 93s1p, manufactured by Deutsche Accumotive). In order to parameterize the thermal model of the traction battery pack we disassembled a battery pack and collected measurements of its size, composition and materials (Figure 7). We parameterized a simplified lumped thermal model (Figure 3) using these measurements, literature values of thermal parameters, a liquid cooling system model and laboratory pack measurements.

Furthermore, we measured the 1-phase and 3-phase charging efficiency of the on-board charger. The maximum efficiency of 93% was reached with a charging power of 11 kW. We also measured the delay between setting a new charging current limitation via the charging cable and the time when the new charging current is reached. On average it took 52 s to reach a higher charging current by the EV and 4 s to reach a lower charging current.

We carried out extensive aging tests on the battery cells to measure the aging trends due to calendar and cyclic aging. We observed accelerated calendar aging at high temperatures and SOC above 75%. A linear function of time fit the measurement data of capacity and inner resistance during the aging test. Cells stored at 100% SOC and 40 °C reached end-of-life (80% of initial capacity) after 431–589 days. In the cycle aging test, the first cell to reach end-of-life had been cycled with a DOD of 95% around a mean SOC of 50%. The end-of-life was reached in the range of 2649 EQFC to 2849 EQFC. An EQFC of 2649 is equivalent to a driving distance of over 306,000 km for an average consumption of 15.2 kWh/100 km. However, this DOD is not achievable in the Smart e.d. as the BMS limits the SOC range between 3.2% and 95.3%. The maximum DOD that could be reached is therefore 92.1% and would also only be reached in V2G applications as drivers would not take the risk to fully discharge the battery. The second cell to reach EOL is the cell that was cycled with 80% DOD around an SOC of 50%. The EOL is reached after 3634 EQFC which equates to a driving distance of over 420,000 km. Higher DODs lead to accelerated aging of the battery cells but overall the impact of cycle aging of the Li-Tec cell of the Smart e.d. is small compared to the impact of calendar aging. This holds especially true if the EV is primarily used for mobility. In V2G applications, such as energy trading, participation in reserve markets or grid boosting the cycle life might play a larger role. In the primary use case of mobility calendar, aging is the dominant aging factor for the traction battery pack studied in this paper.

The complete traction battery model was validated using laboratory pack measurement tests and measured battery data collected during driving tests via the CAN-Bus of the Smart. The simulation results of the parameterized EV model showed good agreement with the validation data. The RMSE of the cell voltage was between 18.49 mV and 67.17 mV for the laboratory pack and the EV operation tests. The RMSE of the pack temperature was between 1.05 K and 1.99 K for the laboratory pack tests.

The full parameter set of the traction battery model is provided in Appendix A. The model presented here is specifically suited to serve as a resource for vehicle-to-grid strategy development as it accurately describes the relevant components of the EV and charger for vehicle-to-grid applications.

Author Contributions: Conceptualization, F.R., I.S. and J.F.; methodology, F.R., I.S., T.W. and A.C.; software, F.R., T.W., A.C. and F.H.; validation, F.R., A.C. and P.D.; formal analysis, F.R., E.B. and F.H.; investigation, F.R., I.S., T.W. and M.K.; writing—original draft preparation, F.R. and T.W.; writing—review and editing, I.S., A.C., M.K. and J.F.; visualization, F.R. and J.F.; supervision, D.U.S.; project administration, F.R., I.S. and D.U.S.; funding acquisition, D.U.S. All authors have read and agreed to the published version of the manuscript.

Funding: The project upon which this publication is based was funded by the German Federal Ministry of Transport and Digital Infrastructure under project number 16SBS001C.

Data Availability Statement: Not applicable.

Conflicts of Interest: The authors declare no conflict of interest.

Abbreviations

The following abbreviations are used in this manuscript:

AC	Alternating Current
BMS	Battery Management System
CCS	Combined Charging System
CC	Constant Current
CP	Control Pilot
CV	Constant Voltage
DC	Direct Current
DOD	Depth-of-Discharge
DSO	Distribution System Operator
ECD	Equivalent Circuit Diagram
ECM	Equivalent Circuit Model
EOL	End-of-life
EQFC	Equivalent full Cycles
EV	Electric Vehicle
EU	European Union
ISEA	Institute for Power Electronics and Electrical Drives
GHG	Greenhouse Gas
LFP	Lithium-Iron-Phosphate
LMO	Lithium-Manganese-Oxide
NCA	Nickel-Cobalt-Aluminum
NMC	Nickel-Manganese-Cobalt
OCV	Open Circuit Voltage
P2D	Pseudo-two-dimensional
PWM	Pulse-width Modulation
PSO	Particle Swarm Optimization
RMSE	Root Mean Square Error
SECC	Supply Equipment Communication Controller
SEI	Solid Electrolyte Interface
SOC	State of Charge
TIM	Thermal Interface Material
TSO	Transmission System Operator
UDSS	Urban Dynamometer Driving Schedule
UPS	Uninterruptible Power Supply
V2G	Vehicle-to-Grid
WLTP	World Harmonized Light-duty Vehicle Test Procedure

Appendix A

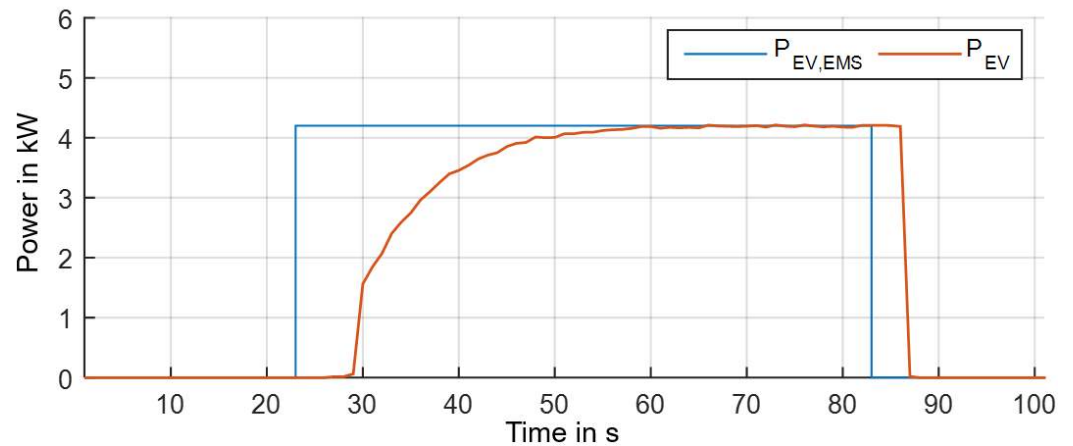


Figure A1. Measurement of charging power control. $P_{EV,EMS}$ is the power requested by the EMS and P_{EV} is the charging power of the EV.

Table A1. Values for parameter C_1 in F of electrical model shown in Figure 2 in dependence of cell temperature and SOC.

SOC	−15 °C	−5 °C	5 °C	15 °C	25 °C	35 °C
0	6.2036	7.9584	7.4502	13.0975	7.3923	67.3145
5	6.7057	7.9584	7.0831	12.0634	7.6907	52.7914
10	7.0351	7.9058	8.1745	9.7993	9.7993	31.2679
15	7.0362	7.7804	8.2376	8.5921	8.5921	20.3526
20	7.025	7.6302	7.8927	7.8728	7.8728	15.4208
25	7.0074	7.5035	7.6377	7.4329	7.4329	12.8902
30	6.9953	7.3938	7.4458	7.1292	7.1292	11.4807
35	6.9859	7.321	7.3006	6.9232	6.9232	10.5764
40	6.9818	7.2501	7.1929	6.766	6.766	9.9806
45	6.9876	7.2037	7.1078	6.647	6.647	9.6004
50	6.9984	7.1727	7.0403	6.5529	6.5529	9.2664
55	7.0174	7.1526	6.9983	6.4947	6.4947	9.1936
60	7.0358	7.1427	6.9704	6.4468	6.4468	8.8458
65	7.0524	7.1361	6.9536	6.4166	6.4166	8.6808
70	7.0797	7.1536	6.9604	6.4035	6.4035	11.7327
75	7.1131	7.1699	6.9866	6.4153	6.4153	8.769
80	7.1384	7.2062	7.0192	6.44	6.44	8.891
85	7.1669	7.2432	7.0495	6.4431	6.4431	8.9094
90	7.2004	7.272	7.0808	6.4539	6.4539	8.9672
95	7.2463	7.3147	7.1279	6.4731	6.4731	9.121
100	7.2979	7.4146	7.2229	6.5136	8.3874	9.2603

Table A2. Values for parameter C_2 in F of electrical model shown in Figure 2 in dependence of cell temperature and SOC.

SOC	−15 °C	−5 °C	5 °C	15 °C	25 °C	35 °C
0	4141.5919	4286.6052	5516.4437	2118.5361	60.0993	5531.9622
5	5022.3094	4286.6052	6159.9236	3033.2749	58.1937	6678.5867
10	5708.5295	4697.046	7798.3847	4918.0826	4918.0826	9448.3505
15	6041.7281	5284.4166	8813.2291	6317.1787	6317.1787	11,285.6717
20	6374.0387	5884.8955	9432.6452	7257.1822	7257.1822	12,596.6965
25	6708.384	6360.1984	9963.4325	7980.8923	7980.8923	13,341.3285
30	6518.6387	6706.3331	10,449.2833	8444.132	8444.1321	13,997.3891
35	6397.0799	7245.0718	10,766.5061	8976.0607	8976.0606	14,755.9898
40	6431.3843	7358.5873	10,865.4071	9414.1746	9414.1746	15,398.4024
45	6525.6152	7433.5444	10,937.0734	9504.4511	9504.451	16,183.0849
50	6657.4635	7507.8527	11,099.9621	9544.943	9544.943	16,387.729
55	6923.1851	7640.8721	11,096.09	9674.996	9674.996	17,946.6885
60	7163.0191	7773.424	11,214.6962	9685.1701	9685.1701	16,451.9069
65	7360.0617	7546.9592	11,164.4429	9733.1104	9733.1105	16,327.2941
70	7291.066	7660.2968	11,049.7543	9769.1101	9769.1101	19,108.3983
75	7107.4896	7490.5601	10,869.0289	9647.1047	9647.1047	18,348.4586
80	7378.1886	7369.5919	11,006.2558	9745.2247	9745.2247	16,253.7877
85	7507.6149	7374.4778	11,587.7219	10,077.6235	10,077.6234	16,871.9588
90	7317.6989	7519.7098	12,025.6155	10,226.4339	10,226.4339	17,445.8639
95	7615.8306	7787.3085	12,402.6332	10,509.1678	10,509.1677	17,726.0212
100	8229.7746	8162.5097	12,688.7936	10,981.5609	63.7065	18,549.9549

Table A3. Values for parameter R_1 in Ω of electrical model shown in Figure 2 in dependence of cell temperature and SOC.

SOC	−15 °C	−5 °C	5 °C	15 °C	25 °C	35 °C
0	0.080049	0.022681	0.0075994	0.0031085	0.0016543	0.00083272
5	0.080813	0.022681	0.0074289	0.0029965	0.0016361	0.00072845
10	0.081019	0.022443	0.0072283	0.0027771	0.0027771	0.00055252
15	0.080114	0.02204	0.0069696	0.0026011	0.0026011	0.00047537
20	0.079403	0.02157	0.0067263	0.0024714	0.0024714	0.00043031
25	0.07879	0.021096	0.006519	0.0023783	0.0023783	0.00040173
30	0.077989	0.020618	0.0063371	0.0022976	0.0022976	0.00037995
35	0.07717	0.020242	0.0061748	0.0022282	0.0022282	0.00036301
40	0.076315	0.019882	0.0060269	0.0021654	0.0021654	0.00034835
45	0.075792	0.01956	0.0059057	0.0021135	0.0021135	0.00033465
50	0.075435	0.019288	0.0058104	0.0020704	0.0020704	0.00032324
55	0.074636	0.019064	0.0057405	0.0020316	0.0020316	0.00031829
60	0.073822	0.01886	0.0056725	0.0019981	0.0019981	0.00030497
65	0.072979	0.018613	0.005597	0.0019707	0.0019707	0.00029527
70	0.071834	0.018422	0.0055279	0.0019368	0.0019368	0.00040059
75	0.070536	0.018181	0.0054476	0.0019037	0.0019037	0.00028212
80	0.068815	0.017865	0.0053462	0.0018703	0.0018703	0.00027528
85	0.067044	0.01751	0.0052494	0.0018425	0.0018425	0.00026975
90	0.065175	0.017177	0.0051842	0.0018259	0.0018259	0.00026606
95	0.064342	0.01697	0.0051215	0.0018122	0.0018122	0.00026224
100	0.063995	0.017087	0.005135	0.0017995	0.00025511	0.00026057

Table A4. Values for parameter R_2 in Ω of electrical model shown in Figure 2 in dependence of cell temperature and SOC.

SOC	−15 °C	−5 °C	5 °C	15 °C	25 °C	35 °C
0	0.017962	0.0064332	0.0053752	0.0022864	0.0024531	0.0013569
5	0.018272	0.0064332	0.0050855	0.0018491	0.0020993	0.0010403
10	0.018677	0.0064312	0.0051359	0.0016798	0.0016798	0.00078285
15	0.019272	0.0063328	0.0051021	0.001635	0.001635	0.00067566
20	0.019571	0.0062175	0.0050268	0.0016498	0.0016498	0.00064434
25	0.019723	0.0061373	0.0049072	0.0016547	0.0016547	0.00062327
30	0.018976	0.0060186	0.0047806	0.0016445	0.0016445	0.0006072
35	0.018648	0.0060566	0.0047452	0.0016123	0.0016123	0.00059305
40	0.019136	0.0059892	0.0047685	0.0015945	0.0015945	0.00058318
45	0.01889	0.0060495	0.0047247	0.0016043	0.0016043	0.00058044
50	0.018277	0.0060949	0.0047132	0.0016106	0.0016106	0.00058404
55	0.01845	0.0061307	0.0047856	0.0016312	0.0016312	0.00066865
60	0.018579	0.0061718	0.0048406	0.0016228	0.0016228	0.00060349
65	0.018618	0.005976	0.0048874	0.0016475	0.0016475	0.00061131
70	0.019384	0.0059645	0.00508	0.0016698	0.0016698	0.00083064
75	0.020515	0.0061409	0.0052437	0.001762	0.001762	0.0008464
80	0.019859	0.0062924	0.0051007	0.001704	0.001704	0.0007167
85	0.01902	0.0060444	0.0047286	0.0016229	0.0016229	0.00069362
90	0.017825	0.0055591	0.0044844	0.0015623	0.0015623	0.00068559
95	0.016545	0.0053424	0.0043247	0.0015262	0.0015262	0.00068296
100	0.015225	0.0050156	0.0043414	0.0014648	0.00043849	0.00070003

Table A5. Values for parameter R_{ser} in Ω of electrical model shown in Figure 2 in dependence of cell temperature and SOC.

SOC	−15 °C	−5 °C	5 °C	15 °C	25 °C	35 °C
0	0.0023895	0.0018717	0.0011043	0.00092052	0.00072483	0.00066083
5	0.002708	0.0018717	0.0010703	0.00089389	0.00073228	0.00063753
10	0.0029141	0.0018574	0.0011518	0.00083587	0.00083587	0.00059699
15	0.0028961	0.0018258	0.0011529	0.00079821	0.00079821	0.00056968
20	0.0028806	0.0017895	0.0011236	0.00077344	0.00077344	0.00055148
25	0.0028664	0.0017592	0.0011007	0.00075798	0.00075798	0.00053972
30	0.0028439	0.0017321	0.0010823	0.00074604	0.00074604	0.00053164
35	0.0028218	0.0017115	0.0010676	0.00073729	0.00073729	0.00052591
40	0.0028001	0.0016923	0.0010559	0.00072961	0.00072961	0.00052104
45	0.0027863	0.0016799	0.0010462	0.00072353	0.00072353	0.00051694
50	0.0027766	0.0016695	0.0010386	0.0007186	0.0007186	0.00051324
55	0.0027659	0.0016603	0.0010338	0.00071487	0.00071487	0.00051207
60	0.0027513	0.001653	0.0010291	0.00071147	0.00071147	0.00050736
65	0.0027293	0.001643	0.0010244	0.00070907	0.00070907	0.00050419
70	0.0027054	0.001637	0.0010215	0.0007063	0.0007063	0.0005252
75	0.0026805	0.0016297	0.0010183	0.00070426	0.00070426	0.00049973
80	0.0026493	0.0016201	0.0010142	0.00070208	0.00070208	0.00049713
85	0.0026158	0.0016098	0.0010108	0.00070045	0.00070045	0.00049454
90	0.0025779	0.0016007	0.0010086	0.00069938	0.00069938	0.00049214
95	0.0025621	0.0015961	0.0010072	0.00069868	0.00069868	0.00048918
100	0.0025566	0.0016054	0.0010105	0.0006979	0.00054062	0.00048606

Table A6. Values for parameter OCV in V of electrical model shown in Figure 2 in dependence of cell temperature and SOC.

SOC	−5 °C	5 °C	15 °C	25 °C	35 °C
−5	3.3785	3.4228	3.4152	3.2082	3.1035
0	3.4064	3.4481	3.4427	3.3287	3.3076
5	3.4342	3.4734	3.4703	3.4477	3.4526
10	3.4621	3.4987	3.4978	3.4963	3.498
15	3.49	3.524	3.5254	3.5223	3.5229
20	3.5178	3.5494	3.5523	3.5498	3.5499
25	3.5457	3.5746	3.577	3.5754	3.5748
30	3.5735	3.5965	3.5991	3.5974	3.5967
35	3.6014	3.6194	3.6234	3.6214	3.6204
40	3.6292	3.6427	3.6485	3.6498	3.6496
45	3.6571	3.6648	3.6702	3.6715	3.6749
50	3.685	3.6884	3.6927	3.6936	3.6978
55	3.7128	3.715	3.7192	3.7201	3.7241
60	3.7451	3.7469	3.7509	3.7516	3.7553
65	3.7825	3.7839	3.7887	3.7892	3.7922
70	3.8254	3.8274	3.8313	3.8316	3.8341
75	3.8746	3.8751	3.8789	3.8794	3.8805
80	3.9326	3.9303	3.934	3.9357	3.9342
85	3.9954	3.996	3.9978	3.998	3.9966
90	4.0589	4.0586	4.0584	4.0574	4.0564
95	4.1242	4.1209	4.1198	4.1176	4.1165
100	4.1862	4.1862	4.1862	4.1835	4.1816
105	4.1862	4.1862	4.1862	4.1862	4.1862

References

1. European Commission. *A European Strategy for Low-Emission Mobility, SWD(2016) 244 Final*; European Commission: Brussel, Belgium, 2016.
2. European Commission Eurostat, Energy Dashboard. Available online: https://ec.europa.eu/eurostat/cache/infographs/energy_dashboard/endash.html (accessed on 10 October 2021).
3. IEA. *Global EV Outlook 2020*; Technical Report; International Energy Agency: Paris, France, 2020.
4. Infas Institut für Angewandte Sozialwissenschaft GmbH. *Mobilität in Deutschland 2017-Ergebnisbericht*; Infas Institut für Angewandte Sozialwissenschaft GmbH: Bonn, Germany, 2017.
5. Osieczko, K.; Zimon, D.; Płaczek, E.; Prokopiuk, I. Factors that influence the expansion of electric delivery vehicles and trucks in EU countries. *J. Environ. Manag.* **2021**, *296*, 113177. [[CrossRef](#)]
6. Englberger, S.; Abo Gamra, K.; Tepe, B.; Schreiber, M.; Jossen, A.; Hesse, H. Electric vehicle multi-use: Optimizing multiple value streams using mobile storage systems in a vehicle-to-grid context. *Appl. Energy* **2021**, *304*, 117862. [[CrossRef](#)]
7. Heilmann, C.; Friedl, G. Factors influencing the economic success of grid-to-vehicle and vehicle-to-grid applications—A review and meta-analysis. *Renew. Sustain. Energy Rev.* **2021**, *145*, 111115. [[CrossRef](#)]
8. Golmohamadi, H. Virtual storage plants in parking lots of electric vehicles providing local/global power system support. *J. Energy Storage* **2021**, *43*, 103249. [[CrossRef](#)]
9. Wang, Y.; Tian, J.; Sun, Z.; Wang, L.; Xu, R.; Li, M.; Chen, Z. A comprehensive review of battery modeling and state estimation approaches for advanced battery management systems. *Renew. Sustain. Energy Rev.* **2020**, *131*, 110015. [[CrossRef](#)]
10. Mesbahi, T.; Sugrañes, R.B.; Bakri, R.; Bartholomeüs, P. Coupled electro-thermal modeling of lithium-ion batteries for electric vehicle application. *J. Energy Storage* **2021**, *35*, 102260. [[CrossRef](#)]
11. Li, Y.; Li, K.; Xie, Y.; Liu, B.; Liu, J.; Zheng, J.; Li, W. Optimization of charging strategy for lithium-ion battery packs based on complete battery pack model. *J. Energy Storage* **2021**, *37*, 102466. [[CrossRef](#)]
12. Schmid, M.; Vögele, U.; Endisch, C. A novel matrix-vector-based framework for modeling and simulation of electric vehicle battery packs. *J. Energy Storage* **2020**, *32*, 101736. [[CrossRef](#)]
13. Zhu, R.; Duan, B.; Zhang, C.; Gong, S. Accurate lithium-ion battery modeling with inverse repeat binary sequence for electric vehicle applications. *Appl. Energy* **2019**, *251*, 113339. [[CrossRef](#)]
14. Wen, F.; Duan, B.; Zhang, C.; Zhu, R.; Shang, Y.; Zhang, J. High-Accuracy Parameter Identification Method for Equivalent-Circuit Models of Lithium-Ion Batteries Based on the Stochastic Theory Response Reconstruction. *Electronics* **2019**, *8*, 834. [[CrossRef](#)]
15. Irimia, C.; Grovu, M.; Sirbu, G.M.; Birtas, A.; Husar, C.; Ponchant, M. The modeling and simulation of an Electric Vehicle based on Simcenter Amesim platform. In Proceedings of the 2019 Electric Vehicles International Conference (EV), Bucharest, Romania, 3–4 October 2019; pp. 1–6. [[CrossRef](#)]

16. Hosseinzadeh, E.; Genieser, R.; Worwood, D.; Barai, A.; Marco, J.; Jennings, P. A systematic approach for electrochemical-thermal modelling of a large format lithium-ion battery for electric vehicle application. *J. Power Sources* **2018**, *382*, 77–94. [CrossRef]
17. Jafari, M.; Gauchia, A.; Zhao, S.; Zhang, K.; Gauchia, L. Electric Vehicle Battery Cycle Aging Evaluation in Real-World Daily Driving and Vehicle-to-Grid Services. *IEEE Trans. Transp. Electrification* **2018**, *4*, 122–134. [CrossRef]
18. Gao, Y.; Jiang, J.; Zhang, C.; Zhang, W.; Ma, Z.; Jiang, Y. Lithium-ion battery aging mechanisms and life model under different charging stresses. *J. Power Sources* **2017**, *356*, 103–114. [CrossRef]
19. Schmalstieg, J.; Käbitz, S.; Ecker, M.; Sauer, D.U. A holistic aging model for Li(NiMnCo)O₂ based 18,650 lithium-ion batteries. *J. Power Sources* **2014**, *257*, 325–334. [CrossRef]
20. Newman, J.; Tiedemann, W. Porous-electrode theory with battery applications. *Aiche J.* **1975**, *21*, 25–41. [CrossRef]
21. Fuller, T.F.; Doyle, M.; Newman, J. Simulation and optimization of the dual lithium ion insertion cell. *J. Electrochem. Soc.* **1994**, *141*, 1. [CrossRef]
22. Newman, J.; Thomas-Alyea, K.E. *Electrochemical Systems*, 3rd ed.; Wiley-Interscience: New York, NY, USA, 2004.
23. Romero-Becerril, A.; Alvarez-Icaza, L. Comparison of discretization methods applied to the single-particle model of lithium-ion batteries. *J. Power Sources* **2011**, *196*, 10267–10279. [CrossRef]
24. Johnson, V. Battery performance models in ADVISOR. *J. Power Sources* **2002**, *110*, 321–329. [CrossRef]
25. Liaw, B.; Nagasubramanian, G.; Jungst, R.; Doughty, D. Modeling of lithium ion cells—A simple equivalent-circuit model approach. *Solid State Ionics* **2004**, *175*, 835–839. [CrossRef]
26. Mingant, R.; Petit, M.; Belaid, S.; Bernard, J. Data-driven model development to predict the aging of a Li-ion battery pack in electric vehicles representative conditions. *J. Energy Storage* **2021**, *39*, 102592. [CrossRef]
27. Tang, X.; Zou, C.; Yao, K.; Lu, J.; Xia, Y.; Gao, F. Aging trajectory prediction for lithium-ion batteries via model migration and Bayesian Monte Carlo method. *Appl. Energy* **2019**, *254*, 113591. [CrossRef]
28. Tang, X.; Liu, K.; Li, K.; Widanage, W.D.; Kendrick, E.; Gao, F. Recovering large-scale battery aging dataset with machine learning. *Patterns* **2021**, *2*, 100302. [CrossRef] [PubMed]
29. Carlier, D.; Saadoune, I.; Ménétrier, M.; Delmas, C. Lithium Electrochemical Deintercalation from O₂ LiCoO₂: Structure and Physical Properties. *J. Electrochem. Soc.* **2002**, *149*, A1310. [CrossRef]
30. Tran, M.K.; Mevawala, A.; Panchal, S.; Raahemifar, K.; Fowler, M.; Fraser, R. Effect of integrating the hysteresis component to the equivalent circuit model of Lithium-ion battery for dynamic and non-dynamic applications. *J. Energy Storage* **2020**, *32*, 101785. [CrossRef]
31. Tran, M.K.; DaCosta, A.; Mevawalla, A.; Panchal, S.; Fowler, M. Comparative Study of Equivalent Circuit Models Performance in Four Common Lithium-Ion Batteries: LFP, NMC, LMO, NCA. *Batteries* **2021**, *7*, 51. [CrossRef]
32. Zou, C.; Zhang, L.; Hu, X.; Wang, Z.; Wik, T.; Pecht, M. A review of fractional-order techniques applied to lithium-ion batteries, lead-acid batteries, and supercapacitors. *J. Power Sources* **2018**, *390*, 286–296. [CrossRef]
33. Habedank, J.B.; Kraft, L.; Rheinfeld, A.; Krezdorn, C.; Jossen, A.; Zaeh, M.F. Increasing the Discharge Rate Capability of Lithium-Ion Cells with Laser-Structured Graphite Anodes: Modeling and Simulation. *J. Electrochem. Soc.* **2018**, *165*, A1563–A1573. [CrossRef]
34. Yang, R.; Xiong, R.; Shen, W.; Lin, X. Extreme Learning Machine-Based Thermal Model for Lithium-Ion Batteries of Electric Vehicles under External Short Circuit. *Engineering* **2020**, *7*, 395–405. [CrossRef]
35. Ecker, M.; Gerschler, J.B.; Vogel, J.; Käbitz, S.; Hust, F.; Dechent, P.; Sauer, D.U. Development of a lifetime prediction model for lithium-ion batteries based on extended accelerated aging test data. *J. Power Sources* **2012**, *215*, 248–257. [CrossRef]
36. Ecker, M.; Nieto, N.; Käbitz, S.; Schmalstieg, J.; Blanke, H.; Warnecke, A.; Sauer, D.U. Calendar and cycle life study of Li(NiMnCo)O₂-based 18,650 lithium-ion batteries. *J. Power Sources* **2014**, *248*, 839–851. [CrossRef]
37. Lewerenz, M.; Marongiu, A.; Warnecke, A.; Sauer, D.U. Differential voltage analysis as a tool for analyzing inhomogeneous aging: A case study for LiFePO₄/Graphite cylindrical cells. *J. Power Sources* **2017**, *368*, 57–67. [CrossRef]
38. Renganathan, S.; Sikha, G.; Santhanagopalan, S.; White, R.E. Theoretical Analysis of Stresses in a Lithium Ion Cell. *J. Electrochem. Soc.* **2010**, *157*, A155. [CrossRef]
39. Laresgoiti, I.; Käbitz, S.; Ecker, M.; Sauer, D.U. Modeling mechanical degradation in lithium ion batteries during cycling: Solid electrolyte interphase fracture. *J. Power Sources* **2015**, *300*, 112–122. [CrossRef]
40. Arora, P.; Doyle, M.; White, R.E. Mathematical modeling of the lithium deposition overcharge reaction in lithium-ion batteries using carbon-based negative electrodes. *J. Electrochem. Soc.* **1999**, *146*. [CrossRef]
41. Diaz, A.G.J. Advanced Vehicle Testing and Evaluation. Technical Report, Intertek. 2018. Available online: <https://www.osti.gov/servlets/purl/1481912> (accessed on 6 March 2022).
42. Kim, D.H.; Kim, M.J.; Lee, B.K. An Integrated Battery Charger with High Power Density and Efficiency for Electric Vehicles. *IEEE Trans. Power Electron.* **2017**, *32*, 4553–4565. [CrossRef]
43. Radimov, N.; Li, G.; Tang, M.; Wang, X. Three-stage SiC-based bi-directional on-board battery charger with titanium level efficiency. *IET Power Electron.* **2020**, *13*, 1477–1480. [CrossRef]
44. Schram, W.; Brinkel, N.; Smink, G.; van Wijk, T.; van Sark, W. Empirical Evaluation of V2G Round-trip Efficiency. In Proceedings of the 2020 International Conference on Smart Energy Systems and Technologies (SEST), Istanbul, Turkey, 7–9 September 2020; pp. 1–6. [CrossRef]

45. Rajendran, G.; Vaithilingam, C.A.; Mison, N.; Naidu, K.; Ahmed, M.R. A comprehensive review on system architecture and international standards for electric vehicle charging stations. *J. Energy Storage* **2021**, *42*, 103099. [CrossRef]
46. Dini, P.; Saponara, S. Electro-Thermal Model-Based Design of Bidirectional On-Board Chargers in Hybrid and Full Electric Vehicles. *Electronics* **2021**, *11*, 112. [CrossRef]
47. Andersen, P.B.; Togholjerdi, S.H.; Sörensen, T.M.; Christensen, B.E.; Lodberg Høj, J.C.M.; Zecchino, A. The Parker Project 2019. Available online: https://parker-project.com/wp-content/uploads/2019/03/Parker_Final-report_v1.1_2019.pdf (accessed on 6 March 2022).
48. Arnold, G.; Brandl, R.; Degner, T.; Gerhardt, N.; Landau, M.; Nestle, D.; Portula, M.; Scheidler, A.; Schwinn, R.; Baumbusch, K.; et al. Intelligente Netzanbindung von Elektrofahrzeugen zur Erbringung von Systemdienstleistungen—INEES. Technical report, Fraunhofer IWES, LichtBlick SE, SMA AG, Volkswagen AG, 2018. Available online: https://www.erneuerbar-mobil.de/sites/default/files/2016-09/INEES_Abschlussbericht.pdf (accessed on 6 March 2022).
49. Degner, T.; Arnold, G.; Brandl, R.; Dollichon, J.; Scheidler, A. Grid Impact of Electric Vehicles with Secondary Control Reserve Capability. In Proceedings of the 1st E-Mobility Power System Integration Symposium, Berlin, Germany, 24–27 October 2017.
50. Daimler, A.G. Available online: <https://media.daimler.com/marsMediaSite/ko/en/9920260> (accessed on 20 April 2020).
51. Daimler, A.G. Introduction of the Smart Fortwo ELECTRIC Drive (3rd Generation) Model Series 451: Introduction into Service Manual; Technical Report. Available online: https://moba.i.mercedes-benz.com/markets-smart/ece-row/baix/cars/smart-fortwo-ed-451/en_GB/downloads/BA_smart_451_ECE_ev_AEJ2014_en_GB.pdf (accessed on 6 March 2022)
52. Li-Tec Battery GmbH. MS-TD-058 *Technisches Datenblatt HEA 50*; Rev. 2.0; Technical Report; Li-Tec Battery GmbH: Kamenz, Germany, 2015.
53. Witzhausen, H. Elektrische Batteriespeichermodelle: Modellbildung, Parameteridentifikation und Modellreduktion; 1. Auflage. Ph.D. Thesis, RWTH Aachen University, Aachen, Germany, 2017. [CrossRef]
54. Abada, S.; Marlair, G.; Lecocq, A.; Petit, M.; Sauvart-Moynot, V.; Huet, F. Safety focused modeling of lithium-ion batteries: A review. *J. Power Sources* **2016**, *306*, 178–192. [CrossRef]
55. Schmidt, J.P. Verfahren zur Charakterisierung und Modellierung von Lithium-Ionen Zellen. Ph.D. Thesis, Karlsruhe Institute for Technologie, Institute for applied materials - Electrochemical Technologies, Karlsruhe, Germany, 2013. [CrossRef]
56. Hu, X.; Li, S.; Peng, H. A comparative study of equivalent circuit models for Li-ion batteries. *J. Power Sources* **2012**, *198*, 359–367. [CrossRef]
57. Schmalstieg, J. Physikalisch-Elektrochemische Simulation von Lithium-Ionen-Batterien: Implementierung, Parametrierung und Anwendung. Ph.D. Thesis, RWTH Aachen University, Aachen, Germany, 2017. [CrossRef]
58. Zhang, Q.Z.; Wang, X.Y.; Yuan, H.M. Estimation for SOC of Li-ion battery based on two-order RC temperature model. In Proceedings of the 2018 13th IEEE Conference on Industrial Electronics and Applications (ICIEA), Wuhan, China, 31 May–2 June 2018; pp. 2601–2606. [CrossRef]
59. Kumar, M.S.; Manasa, T.R.; Raja, B.; Selvajyothi, K. Estimation of State of Charge and Terminal Voltage of Li-ion Battery using Extended Kalman Filter. In Proceedings of the 2020 6th IEEE International Energy Conference (ENERGYCon), Tunis, Tunisia, 28 September–1 October 2020; pp. 515–520. [CrossRef]
60. Kiel, M. Impedanzspektroskopie an Batterien unter Besonderer Berücksichtigung von Batteriesensoren für den Feldeinsatz. Ph.D. Thesis, RWTH Aachen University, Aachen, Germany, 2013.
61. Bernardi, D.; Pawlikowski, E.; Newman, J. A General Energy Balance for Battery Systems. *J. Electrochem. Soc.* **1985**, *132*, 5–12. [CrossRef]
62. Magnor, D.T. Globale Optimierung netzgekoppelter PV-Batteriesysteme unter besonderer Berücksichtigung der Batteriealterung. Ph.D. Thesis, RWTH Aachen University, Aachen, Germany, 2017. [CrossRef]
63. Hust, F.E. Physico-Chemically Motivated Parameterization and Modelling of Real-Time Capable Lithium-Ion Battery Models: A Case Study on the Tesla Model S battery. Ph.D. Thesis, RWTH Aachen University, Aachen, Germany, 2019. [CrossRef]
64. DLR. Mobilität in Tabellen. 2017. Available online: <https://mobilitaet-in-tabellen.dlr.de/mit/> (accessed on 24 June 2021).
65. Ange-Etienne Acquaviva, Cédric. Development and Validation of a Plant Model for Battery Monitoring Systems (BMS) for High Voltage Batteries. Diploma Thesis, INSA Strasbourg, Strasbourg, France, 2012.
66. Friesen, A.; Horsthemke, F.; Mönnighoff, X.; Brunklaus, G.; Krafft, R.; Börner, M.; Risthaus, T.; Winter, M.; Schappacher, F.M. Impact of cycling at low temperatures on the safety behavior of 18650-type lithium ion cells: Combined study of mechanical and thermal abuse testing accompanied by post-mortem analysis. *J. Power Sources* **2016**, *334*, 1–11. [CrossRef]
67. Ziebert, C.; Uhlmann, N.; Ouyang, S.; Lei, B.; Zhao, W.; Rohde, M.; Seifert, H.J. *Battery Calorimetry of Li-Ion Cells to Prevent Thermal Runaway and Develop Safer Cells*; Technical Report; Karlsruhe Institute of Technology, Institute for Applied Materials: Mainz, Germany, 2018.
68. Baehr, H.D.; Stephan, K. *Wärme- und Stoffübertragung, 9. Auflage*; Springer: Berlin/Heidelberg, Germany; New York, NY, USA, 2016.
69. Downie, D.; Martin, J. An adiabatic calorimeter for heat-capacity measurements between 6 and 300 K. The molar heat capacity of aluminium. *J. Chem. Thermodyn.* **1980**, *12*, 779–786. [CrossRef]
70. Weidenfeller, B.; Höfer, M.; Schilling, F.R. Thermal conductivity, thermal diffusivity, and specific heat capacity of particle filled polypropylene. *Compos. Part A Appl. Sci. Manuf.* **2004**, *35*, 423–429. [CrossRef]

71. Baumhöfer, T.; Brühl, M.; Rothgang, S.; Sauer, D.U. Production caused variation in capacity aging trend and correlation to initial cell performance. *J. Power Sources* **2014**, *247*, 332–338. [[CrossRef](#)]
72. Krupp, A.; Beckmann, R.; Diekmann, T.; Ferg, E.; Schuldt, F.; Agert, C. Calendar aging model for lithium-ion batteries considering the influence of cell characterization. *J. Energy Storage* **2022**, *45*, 103506. [[CrossRef](#)]
73. de Hoog, J.; Timmermans, J.M.; Ioan-Stroe, D.; Swierczynski, M.; Jaguemont, J.; Goutam, S.; Omar, N.; Van Mierlo, J.; Van Den Bossche, P. Combined cycling and calendar capacity fade modeling of a Nickel-Manganese-Cobalt Oxide Cell with real-life profile validation. *Appl. Energy* **2017**, *200*, 47–61. [[CrossRef](#)]